

Elsevier Editorial System(tm) for Marine Geology  
Manuscript Draft

Manuscript Number: MARGO5332R1

Title: Effects of coastal submarine canyons on tsunami propagation and impact

Article Type: Research Paper

Keywords: Tsunami; multi-scenario; numerical simulation; submarine canyon

Corresponding Author: Dr. Galderic Lastras, PhD

Corresponding Author's Institution: Universitat de Barcelona

First Author: Olaia Iglesias, MSc

Order of Authors: Olaia Iglesias, MSc; Galderic Lastras, PhD; Carlos Souto, PhD; Sergio Costa, MSc;  
Miquel Canals, Professor

## **Highlights**

Canyon incision, width and orientation modify tsunami wave arrival and run-up.

Shoreward of a canyon head, tsunami height diminishes with increased incision.

At both sides of the canyon, tsunami wave height increases.

The presence of a canyon incised very close to the coast can produce edge waves.

1

2

3

4

# **Effects of coastal submarine canyons on tsunami propagation and impact**

5

6

7 Olaia Iglesias<sup>a</sup>, Galderic Lastras<sup>a\*</sup>, Carlos Souto<sup>b</sup>, Sergio Costa<sup>a</sup>, Miquel Canals<sup>a</sup>

8

9

10

11 <sup>a</sup> GRC Geociències Marines, Universitat de Barcelona, E-08028, Spain

12 <sup>b</sup> Grupo de Oceanografía Física, Universidade de Vigo, E-36200, Spain

13

14 \*Corresponding author: glastras@ub.edu

15 Tel. +34 934034490

16 Fax. +34 934021340

17

18

19    **Abstract**

20    We analyse the variations produced on tsunami propagation and impact over a straight coastline  
21    because of the presence of a submarine canyon incised in the continental margin. For ease of  
22    calculation we assume that the shoreline and the shelf edge are parallel and that the incident wave  
23    approaches them normally. A total of 512 synthetic scenarios have been computed by combining the  
24    bathymetry of a continental margin incised by a parameterised single canyon and the incident  
25    tsunami waves. The margin bathymetry, the canyon and the tsunami waves have been generated  
26    using mathematical functions (e.g. Gaussian). Canyon parameters analysed are: (i) incision length into  
27    the continental shelf, which for a constant shelf width relates directly to distance from the canyon  
28    head to the coast, (ii) canyon width, and (iii) canyon orientation with respect to the shoreline.  
29    Tsunami wave parameters considered are period and sign. The COMCOT tsunami model from Cornell  
30    University was applied to propagate the waves across the synthetic bathymetric surfaces. Five  
31    simulations of tsunami propagation over a non-canyoned margin were also performed for reference.

32

33    The analysis of the results reveals a strong variation of tsunami arrival times and amplitudes reaching  
34    the coastline when a tsunami wave travels over a submarine canyon, with changing maximum height  
35    location and alongshore extension. In general, the presence of a submarine canyon lowers the arrival  
36    time to the shoreline but prevents wave build-up just over the canyon axis. This leads to a decrease in  
37    tsunami amplitude at the coastal stretch located just shoreward of the canyon head, which results in  
38    a lower run-up in comparison with a non-canyoned margin. Contrarily, an increased wave build-up  
39    occurs on both sides of the canyon head, generating two coastal stretches with an enhanced run-up.  
40    These aggravated or reduced tsunami effects are modified with (i) proximity of the canyon tip to the  
41    coast, amplifying the wave height, (ii) canyon width, enlarging the areas with lower and higher  
42    maximum height wave along the coastline, and (iii) canyon obliquity with respect to the shoreline and  
43    shelf edge, increasing wave height shoreward of the leeward flank of the canyon. Moreover, the  
44    presence of a submarine canyon near the coast produces a variation of wave energy along the shore,

eventually resulting in edge waves shoreward of the canyon head. Edge waves subsequently spread out alongshore reaching significant amplitudes especially when coupling with tsunami secondary waves occurs. Model results have been groundtruthed using the actual bathymetry of Blanes Canyon area in the North Catalan margin. This paper underlines the effects of the presence, morphology and orientation of submarine canyons as a determining factor on tsunami propagation and impact, which could prevail over other effects deriving from coastal configuration.

51

52

### 53 **Keywords**

54 Tsunami; multi-scenario; numerical simulation; submarine canyon

55

### 56 **1. Introduction**

57 Tsunamis are ocean waves produced by vertical seafloor shifts generated as a result of earthquakes, 58 underwater mass failures or volcanic activity, or by the displacement of the water surface due to a 59 significant impact such as a subaerial landslide or a meteorite entering the water body. Their large 60 wavelength in the open ocean and the height they can attain at the coast confer to tsunami waves a 61 known destructive effect. Several strategies have been developed to understand tsunami generation, 62 propagation and impact, so that at the end casualties and infrastructural damage could be minimised. 63 The use of numerical models has emerged as one of the most useful tools for tsunami risk 64 assessment. This approach is particularly valuable given the inability of directly observing the 65 triggering of tsunamis in most cases and their relatively long recurrence periods involving significant 66 gaps in datasets on past tsunamis. Mitigation efforts recently focus on improving forecasting systems 67 for distant tsunamis, based on their detection by specially designed buoys and sets of pre-computed 68 numerical models (Tang et al., 2009), such as the *Short-term Inundation Forecasting for Tsunamis* 69 (SIFT) tool developed by NOAA (Gica et al., 2008).

70

71 The gradual shoreward shallowing of a typical continental margin from the base of slope up to the  
72 continental shelf and coastline produces the decrease of the tsunami wavelength and velocity, and  
73 the increase of height wave, which is known as shoaling effect (Wards, 1989). The significance of this  
74 effect changes according to the particular shape and depth of every slope and shelf. In terms of  
75 tsunami hazard, a wide continental shelf induces a strong shoaling effect that can translate into a late  
76 arrival time to the coastline but also into a larger run-up, that is, the onshore maximum height above  
77 sea level reached by a tsunami.

78

79 Continental slopes and shelves around the world are often incised by submarine canyons i.e. deep  
80 and relatively steep seafloor valleys (see definitions in Daly, 1936; Shepard and Dill, 1966; Normark  
81 and Piper, 1969; Bates and Jackson, 1980; van den Hove and Moreau, 2007). Submarine canyons are  
82 a very common feature in continental margins of the world ocean, with a global average spacing of an  
83 isolated canyon every 21.5 km (Harris and Whiteway, 2011). Recent multibeam bathymetry data have  
84 shown the noticeable morphological variability of submarine canyons (Jobe et al., 2011). The ability  
85 of submarine canyons to modify, enhance and funnel oceanographic processes and flows such as  
86 geostrophic currents, upwelling and downwelling currents, and density flows has been described in  
87 numerous locations and settings (Klinck, 1989; Allen, 2000; Wåhlin, 2002; Canals et al., 2006; Allen  
88 and Hickey, 2010).

89 In this paper, we address the role of submarine canyons and their diverse morphology on tsunami  
90 propagation and subsequent coastal impact, a topic that has been addressed a few times with  
91 contradictory results. For instance, Matsuyama et al. (1999) and Tappin et al. (2001) have considered  
92 that the canyon located on the Sissano Shelf was mostly responsible of high tsunami run-outs on  
93 Sissano Lagoon on 1998. Likewise, Ioualalen et al. (2007) suggested that the submarine canyon off  
94 the Bangladesh shelf produced wave amplification on the Barisal coast of the 2004 Indian Ocean  
95 tsunami. Contrarily, Divyalakshmi et al. (2011) suggested that the presence of Palar canyon produced  
96 a local wave height reduction in the southeast India coast during the same event. Therefore, in order

to shed light on this issue, we evaluate how submarine canyons modify wave arrival times and maximum tsunami wave heights over the adjacent coastline considering a synthetic multi-scenario approach to overcome the difficulty of distinguishing the influence of a submarine canyon from other effects also deriving from shoreline, shelf and slope configuration and related resonance phenomena. This approach also allows isolating and evaluating the effects of each of the parameters under study for each tsunami simulation. As a groundtruthing exercise, we also present the analysis of a hypothetical tsunami impact in an actual bathymetric configuration, the Blanes Canyon area in the North Catalan margin. This allows us assessing the effects due to the canyon against other local effects as mentioned above. The aim of this work is to provide general clues for tsunami hazard and associated risk analysis in canyoned margins.

## **2. Methodology**

### **2.1. Synthetic bathymetries**

To understand the effect of single canyon geometries on tsunami propagation, synthetic bathymetries of canyons with different shapes and orientations were generated jointly with a non-canyoned continental margin segment. An inclined arctangent was used to simulate the non-canyoned margin including continental rise, slope and shelf, defined by the characteristic slope height (i.e. the vertical distance between the shelf edge and the base of slope,  $Sh$ ), slope width (i.e. the horizontal distance from the shelf edge to the base of the slope,  $Sw$ ), and shelf gradient after a reference modern continental margin ( $Ss$ ). The spatial domain (i.e. regional scale) of this study allows discarding the Coriolis effect and using a right handed Cartesian coordinate system with the  $y$ -axis parallel to the coast assumed to be running south to north (Fig. 1). To avoid grid boundary effects, we have extended the  $y$  axis range by running the simulations over additional areas northward and southward of the primary target region, which is the only region we will consider from here onwards (Fig. 1).

Canyon geometry was defined searching a compromise between complexity, so that morphology is as realistic as possible, and simplicity, so that isolating the consequences of parameter variation is straightforward. The typical concave-shaped longitudinal profile of most canyons (Covault et al., 2011; Amblas et al., 2012) was obtained with the negative part of an arctangent placed in the center of the grid. A Gaussian function was used to generate the profile across the canyon, with variable width along canyon following a cosine function. The orientation of the canyon axis was defined multiplying the Gaussian function by a rotation matrix.

The resulting equation allows parameterising a number of variables and subsequently generating a huge amount of bathymetric surfaces according to the number of discrete values chosen for each parameter. An example of synthetic surface is shown in Figure 1. In this study we analyse the effect of three essential canyon parameters: (i) canyon incision into the continental shelf ( $Ci$ ), measured from the nearest shelf edge to the canyon tip; (ii) canyon width ( $Cw$ ), measured over the continental slope; and (iii) orientation of the canyon axis ( $\alpha$ ), measured with respect to the shelf edge strike (i.e. the canyon azimuth) (Fig. 2). Canyon incision is measured perpendicularly to the shelf edge and not necessarily along the canyon axis, so that for a constant incision, canyon length increases with decreasing intersection angles. Other geomorphic characteristics typical of submarine canyons, such as sinuosity and dendricity (Clark and Pickering, 1966; Pirmez et al., 2000; Harris and Whiteway, 2011; Lastras et al., 2011), have been discarded according to the above-mentioned constraints.

#### 2.1.1. Formulation of the synthetic bathymetries

The following notation has been considered to define the surface of the non-canyoned theoretical continental margin  $Z_{NC}(i,j)$  and the canyoned theoretical continental margin  $Z_c(i,j)$ . For a given grid with  $n_x$ ,  $n_y$  cells (i.e.  $n_x+1$  and  $n_y+1$  nodes) and size  $W_x$ ,  $W_y$  in an  $x$  and  $y$  direction respectively (Fig. 1), we define the distance (in m) between each node and the origin as

$$x(i,j) = W_x \left( \frac{i-1}{n_x} \right) \text{ and} \quad (1)$$



$$y(i, j) = Wy \left( \frac{j-1}{ny} \right), \quad (2)$$

being  $i=(1, 2, \dots, nx+1)$ ,  $j=(1, 2, \dots, ny+1)$ ,  $x(1,j)=0$  and  $y(i,1)=0$ .

150

151 The bathymetry of a non-canyoned margin is generated with the following equation of a tilted  
152 arctangent:

$$Z_{NC}(i, j) = \frac{Sh}{\pi} \cdot atan(2 \cdot pa \cdot lx(i, j)) + Ss \cdot Wx \left( \frac{i}{nx+1} \right) - \frac{Sh}{2} + H_E, \quad (3)$$

154 where  $Sh$  is the slope height,  $pa$  ( $pa=\tan(0.8 \cdot 2 \cdot \pi)=3.078$ ) is an horizontal distance factor,  $Ss$  is the  
155 slope of the continental shelf in radians and  $H_E$  is the height of emerged land at the grid limit (i.e.  
156 nodes  $(nx+1, j)$ ).  $lx(i, j)$  in equation (3) is the distance in the  $x$  direction between each node and the  
157 centre of the grid, normalised to the width of the continental slope ( $Sw$ ). This normalised distance  
158 (and  $ly(i, j)$  in the  $y$  direction) is calculated as follows:

$$lx(i, j) = Wx \frac{\left( \frac{i-1}{nx} - \frac{1}{2} \right)}{Sw} \text{ and} \quad (4)$$

$$ly(i, j) = Wy \frac{\left( \frac{j-1}{ny} - \frac{1}{2} \right)}{Sw}. \quad (5)$$

161

162 With equation (3), and using values such as  $Sh=2000$  m,  $Ss=0.2^\circ$ ,  $H_E=200$  m and  $Sw=50$  km (see  
163 section 2.1), the function generating the non-canyoned surface yields a margin with a 13 km wide  
164 continental shelf, a shelf break at 248 m water depth, a maximum gradient of  $5^\circ$  in the continental  
165 slope, and a base of slope located at 1848 m water depth.

166

167 In order to state the equations that define the same margin incised by a parameterised canyon, we  
168 first define a line ( $y=ax+b$ ) through the centre of the grid with an slope ( $a$ ) that corresponds to the  
169 canyon orientation with respect to the  $x$ -axis ( $\theta$ ) in radians, which is the complementary angle to  $\alpha$   
170 (see section 2.1 and Fig.2),  $\theta=(90-\alpha) \cdot \pi/180$ , such that,  $a=\tan(\theta)$ . This line is, in fact, the canyon axis,

lengthened beyond the canyon limits. The distance between the centre of the grid and the orthogonal projection of each node onto this line is given by

$$Pp(i,j) = lx(i,j) \cdot \cos(\beta) + ly(i,j) \cdot \sin(\beta). \quad (6)$$

The bathymetry of a canyoned margin is generated by three different functions according to the value of  $Pp(i,j)$  with respect to certain limits. The first limit is where the canyon starts narrowing at its head and the second the location of the tip of the canyon head. The first one ( $P$ ) is defined as the distance along the canyon axis from the center of the slope to the point where the canyon starts narrowing normalized to  $Sw$ . In this study we define  $P=0$ , that is, the canyon already starts narrowing from the middle of the slope. The second limit ( $Ctp$ ) is calculated also as the distance along the canyon axis from the center of the slope to the tip of the canyon head, normalized to  $Sw$ , as follows:

$$Ctp = \frac{\frac{Ci}{Sw} + 0.5}{\cos(\beta)} \quad (7)$$

where  $Ci$  represents the canyon incision as defined in section 2.1.

Finally, the bathymetry is defined in equations 8 to 10 depending on the value of  $Pp(i,j)$ :

$$Z_C(i,j) = Z_{NC}(i,j) - Dc \cdot e^{\left(\frac{dr \cdot Sw}{\left(\frac{Cw}{2}\right)^v}\right)} \text{ if } Pp(i,j) < P, \quad (8)$$

$$Z_C(i,j) = Z_{NC}(i,j) - Dc \cdot e^{\left(\frac{dr \cdot Sw}{\left(\sqrt{\ln(5) + \cos\left(\pi \frac{1 - (Ctp - Pp(i,j))}{Ctp - P}\right)^5}\right)^v}\right)} \text{ if } P < Pp(i,j) < Ctp, \text{ and} \quad (9)$$

$$Z_C(i,j) = Z_{NC}(i,j) \text{ if } Pp(i,j) > Ctp \quad (10)$$

In these equations, the depth of the canyon ( $Dc$ ) is given by

$$Dc = \frac{Sh}{\pi} \cdot \operatorname{atan}(2 \cdot pa \cdot lx(i,j)) - \frac{2 \cdot Sh}{\pi} \cdot \operatorname{atan}(2 \cdot pa \cdot (Pp(i,j) - Ctp)) + \frac{Sh}{2}, \quad (11)$$

where  $dr(i,j)$  is the distance of each node to the line ( $y=ax+b$ ) for  $b=1$

$$dr(i,j) = \left| \frac{a \cdot lx(i,j) - ly(i,j)}{\sqrt{(a^2+1)}} \right|, \quad (12)$$

$C_w$  is the canyon width (see section 2.1), and  $v$  is a natural even number that accounts for the gradient of the canyon flanks (we have used  $v=6$ ). Note that if  $D_c < 0$ , the canyon would be a positive relief. In order to avoid this, if equation (11) yields  $D_c < 0$ ,  $D_c$  is directly defined as being equal to 0.

Values used for canyon incision ( $C_i$ ) range from 2 to 16 km using 2 km intervals, canyon width ( $C_w$ ) ranges from 6 to 20 km with the same interval, canyon orientation ( $\alpha$ ) varies from  $60^\circ$  to  $90^\circ$  (oblique to perpendicular to the margin) with direction shifts every  $10^\circ$ . This amounts a total of 257 non-canyoned and canyoned bathymetric scenarios.

## **2.2. Reference bathymetry**

The specific values applied to construct the non-canyoned margin surface as well as the value ranges for canyon parameters were chosen to actually match a real world margin segment, which is the Blanes continental margin that is incised by a large submarine canyon. The Blanes continental margin and canyon are located in the North Catalan margin of the Western Mediterranean Sea (Canals et al., 2004; Amblas et al., 2006; Lastras et al., 2011).

The Blanes margin has an up to 20 km wide, and up to  $0.5^\circ$  in gradient continental shelf. The shelf edge is located at 140 m. The continental slope is rarely steeper than  $4^\circ$  in gradient and the continental rise reaches up to 2600 m in depth (Amblas et al., 2006). The Blanes Canyon is 12 km wide measured on the edge of the slope and its head is incised 14 km into the shelf, with the canyon tip located at less than 5 km from the coastline (Amblas et al., 2006; Lastras et al., 2011). Its axis is slightly oblique ( $65^\circ$ ) to the coastline and to the general trend of the shelf edge. This overall setting is similar to other terrigenous passive margins in the world ocean (Harris and Whiteway, 2011).

A synthetic bathymetry with the canyon erased by interpolation between adjacent off-canyon areas was also constructed after the Blanes margin actual bathymetry. The Blanes margin is then utilized in

the simulations to evaluate the relative significance of canyon effects against other local effects. The Blanes margin bathymetry data used is from Canals et al. (2004).

### **2.3. Synthetic tsunami waves**

Earthquake and landslide-generated tsunami waves have a dipole-shaped profile as a result of the perturbation of the equilibrium surface produced by the vertical displacement of the seabed. Therefore, a simple dipole has been used as incident wave, propagating shoreward from the far field without any perturbation until it arrives to the target region. The ideal wave time profile results from the product between an arctangent function and a single exponential pulse, thus allowing parameterising tsunami period, amplitude and sign. In the simulations, we consider the arrival of distant tsunamis, for which refraction with the seabed produces a wave front parallel to the continental margin.

Synthetic tsunami waves generated in this study have periods ranging ( $P$ ) from 20 to 50 min, using 10 min intervals, which embrace the range of typical tsunami wave periods (Lipa et al., 2011). This is also within the range of periods measured by open ocean buoys during large-scale recent tsunamis. For instance, the tsunami generated by the 2010 Chile earthquake (Mw 8.8) had periods ranging between 20 and 30 min (NOAA, 2012a); the tsunami generated by the 2011 Tohoku or Great East Japan earthquake (Mw 9.0) had periods between 20 and 50 min (NOAA, 2012a; 2012b); the periods of the tsunami triggered by the 2003 Boumerdès-Zemmouri earthquake (Mw 6.8) offshore Algeria were ~17 min (Sahal et al., 2009); and the recorded waves produced by the 2004 Indonesian Sumatra Earthquake (Mw 9.0) had periods ranging from 40 to 120 min (Merrifield et al., 2005). Tsunami waves with the selected periods were applied to the non-canyoned margin whereas only waves with a period of 20 min were run over the canyoned synthetic bathymetries to discard larger wave periods closer to the natural periods of oscillation of the synthetic non-canyoned margin (see detailed explanation in Results and Discussion).

246

247 The sign ( $S$ ) (i.e. positive or negative amplitude of the first arrival) of the tsunami wave measured in a  
248 given point is defined by its location with respect to the tsunami source. We define positive sign  
249 when the crest arrives first, and negative when the trough arrives first. One negative and four positive  
250 waves were considered in this study.

251

252 Variations in incident wave amplitude ( $A$ ) have not been considered as a single value of amplitude is  
253 enough to unveil the effects, in terms of wave height distribution, produced in tsunami propagation  
254 due to the change of canyon parameters. Most amplitude values recorded by open ocean buoys  
255 (NOAA, 2012a) during tsunami events range around 1-10 cm, although extreme values up to a few  
256 meters were registered during the 2004 Indian Ocean tsunami. In our simulations, an amplitude value  
257 of 50 cm has been selected. Tsunami wave time profiles with the values of period, amplitude and sign  
258 used in the simulation are plotted in Figure 3.

259

### 260 2.3.1. Formulation of the tsunami waves

261 Tsunami wave height as a function of time  $h(t)$ , as shown in Figure 3, was calculated following this  
262 equation:

$$263 \quad h(t) = S \cdot \operatorname{atan}\left(\frac{t-b}{\frac{c}{d_0}}\right) \cdot e^{-\left(\frac{(t-b)^2}{\left(\frac{c}{d_0}\right)^2}\right)}, \quad (13)$$

264

265 where  $S$  attributes a sign to the wave (and is thus either 1 or -1),  $t$  is time,  $b$  is half of the wave period  
266 ( $P$ ), the dispersion parameter  $c$  is defined as a quarter of the period ( $P$ ), and  $d_0=1.26$ , which is the  
267 value of  $t$  when height is maximum or minimum. This expression yields an either positive or negative  
268 wave with a maximum amplitude of 0.374.

269

270 Wave height is then normalized to the chosen amplitude ( $A=0.50$  m):

$$H(t) = A \cdot \frac{h(t)}{0.374}. \quad (14)$$

272

## 273 **2.4. Tsunami numerical model**

274 The model used to propagate the tsunami waves across the synthetic bathymetric surfaces is  
 275 COMCOT version 1.7 of Cornell University (Wang, 2009). This model uses an explicit leap-frog finite  
 276 difference scheme to solve linear and non-linear Continuity and Shallow Water Equations (SWE).  
 277 Applying the wave maker option, the model sends into the numerical domain the customized tsunami  
 278 wave. At shallow water depths close to the coast, non-linear and bottom friction effects considerably  
 279 increase. Therefore, we have used non-linear SWE to compute the flow motion. A constant Manning  
 280 roughness coefficient of 0.013 has been applied to describe bottom friction for the entire domain,  
 281 since this value is normally used to describe a typical seabed (Li et al., 2012; Wu et al., 2008). For  
 282 each of the scenarios combining bathymetric surfaces and tsunami waves, 90 min of wave  
 283 propagation were computed, obtaining wave height at each node every 60 s ( $H(i,j,t)$ ). A time step of  
 284 0.4 s was used, thus satisfying the Courant Condition. Boundary conditions along offshore limits of  
 285 the bathymetric grid were set up to “wall”, but reflections were ignored by using a larger grid as  
 286 explained in section 2.1; free water surface was also calculated over the initially dry cells onshore,  
 287 thus allowing the tsunami to unrestrictedly inundate and backwash emerged land. The large  
 288 computational time required to run the COMCOT model for such a large number of scenarios was  
 289 solved by means of parallel computing using Bourne shell scripts that allowed simultaneously running  
 290 several scenarios.

291

## 292 **3. Results and Discussion**

### 293 **3.1. Control simulations**

294 The spectral signature of a tsunami wave depends on the characteristics of the initial wave, which is  
 295 in turn determined by the generation mechanism, and also by the morphological configuration of the  
 296 basin and margin (Rabinovich, 2009). This configuration defines the normal mode, i.e. its resonance

frequencies, and other effects such as shoaling, which can strongly change the impact over the coast, as for the earthquake-generated tsunamis of 2010 in Chile, 2009 in Samoa and 2006 in the Kuril Islands (Yamazaki and Cheung, 2011). Therefore, to characterize such effects in our synthetic margin we first performed control simulations by propagating four positive waves with the selected periods of 20, 30, 40 and 50 min over the non-canyoned bathymetry (Fig. 4A).

Without resonance effects, an increase in wave height with decreasing depth due to shoaling should be expected, with highest waves over the shelf and along the coastline. The distribution of maximum wave heights (MWH) at each cell during these control runs showed that this was the case for the 20 min period wave (Fig. 4A). Contrarily, for the other periods considered, waves over the slope were higher than those over the shelf (Fig. 4A), indicating resonance effects with these wave periods. We have also calculated the power spectral density using the Fast Fourier Transform of the time series recorded in a synthetic station located at the coastline (Fig. 4B). The results show a coincident pattern for the four control simulations, but energy content increases noticeably for tsunami wave periods larger than 20 min. This suggests that tsunamis with the larger wave periods are closer to the natural periods of oscillation of the synthetic non-canyoned margin. With these wave periods, trapped waves can be generated close to the shoreline and over the slope, as suggested by Cutchin and Smith (1973) and Takeda (1984). Since our aim was to characterize the effects due to canyon morphology and minimize other signals, we discarded these wave periods, thus using only the 20 min period in subsequent computations.

### **3.2. Synthetic scenarios**

A total of 514 synthetic scenarios have been computed combining two tsunami waves of opposite signs with a fixed period of 20 min and an amplitude of 0.5 m, with the generated 256 different canyoned bathymetries and the non-canyoned one. An example of the data obtained for a single scenario is shown in Figure 5. It consists of the MWH plot, i.e. the highest wave recorded at every cell

during the entire computation (Fig. 5A), the time series of 21 synthetic tide gauges located along the 10 m isobath close to the coastline spaced every 5 km (Fig. 5B), and the plots of wave height distribution at every time step (1 min) of the computation time (90 min) (Fig 5C). Other subproducts that could be extracted from the processed data are not shown or discussed for ease of concision.

### **3.2.1. First arrivals**

The time of the first arrival to each of the 21 tide gauges for every one of the 514 scenarios has been extracted and plotted in Figure 6. Arrival times correspond to the moment when the synthetic tide gauges record the first positive peak. Therefore, the noticeable difference in arrival times between positive and negative incident waves is produced because the positive peak of the negative wave is preceded by the wave trough. For the non-canyoned margin, the first positive peak arrives to the coast after 28 min for a positive wave and 34 min for a negative wave.

The presence of a submarine canyon results, in general terms, in shorter arrival times shoreward of its head (Fig. 6) and in relative delays sideward. These differences become more pronounced with negative incident waves. While the arrival times of positive waves range between 21 and 28 min, those of negative waves range between 26 and 36 min for specific configurations. Larger canyon incision and width produces shorter arrival times shoreward of the canyon head due to a reduced shoaling effect. Increasing canyon obliquity leads to marked differences in arrival times along the coastline (Fig. 6).

### **3.2.2. Maximum wave height at the coastline**

The distribution of lower and higher MWH along the coastline is a useful criterion in terms of hazard analysis, which is often utilized to establish worst-case scenarios since it is the most determining factor of tsunami run-up and inundation.



MWH values have been extracted from each of the 514 scenarios along the 10 m isobath, i.e. at a 100 m constant distance from the coastline. The values thus obtained are consecutively displayed in Figure 7 following the same height colour scale. Considerable differences in MWH along the 10 m isobath can be observed between non-canyoned and canyoned synthetic bathymetries (Fig. 7). In general, the presence of a submarine canyon leads to lower MWH in the coastal stretch just shoreward of the canyon head, in agreement with the conclusion of Divyalakshmi et al. (2011), with higher values at both sides of that stretch (Fig. 7). These higher MWH values could account for the amplification effects on Barisal coast, Bangladesh, of the 2004 Indian Ocean tsunami described by Ioualalen et al. (2007) and the higher waves recorded at Sissano Lagoon during the 1998 Papua-New Guinea tsunami (Matsuyama et al., 1999; Tappin et al., 2001). Imran (1953) found similar results for long period wind waves in front of La Jolla and Scripps submarine canyons, with higher waves reported at beach stations located between the canyons, and lower waves at those located in front of the canyon heads.

MWH decrease and enhancement ratios shoreward of the canyon, as well as their distribution and symmetry, are largely dependent on canyon morphometry (Fig. 7). The sign of the incident wave strongly determines MWH, with higher values produced by negative amplitude waves in all cases. Furthermore, negative amplitude waves intensify wave height variations because of the presence of the canyon (Fig. 7). This could be explained because the initial trough produces a first decrease in water depth that generates in turn a greater shoaling effect in shallower shelf areas compared to those within the canyon. The effects of canyon incision, width and orientation are described in the following paragraphs.

For a canyon normal to the shoreline (i.e. 90° orientation) with a constant width of 14 km, decreased MWH in the coastal region shoreward of the canyon head get even more reduced with increasing canyon incision (Fig. 8). For instance, a canyon incised 2 km landward of the shelf break results in a

MWH 20% reduction compared to a non-canyoned margin (i.e. from 2.5 to of 2 m MWH). MWH reduction reaches 48% when an incision of 16 km is considered (Fig. 8). In contrast, higher MWH at both sides of the canyon are considerably enhanced. A 2 km incised canyon produces a 4% MWH increase, with MWH attaining 2.6 m. If an incision of 16 km is considered, then the off canyon MWH increases by 12%. The relationship between canyon incision length and MWH decrease in the region shoreward of the canyon head and increase at both sides of the canyon is linear (Fig. 8).

Wave refraction against the canyon walls results in a curved wave front over the canyon head that is later refracted by the shoaling continental shelf. A long distance between the canyon head and the coastline allows the curved wave to be refracted by the continental shelf before hitting the coast, and thus the front wave becomes normal to the coast. On the contrary, if the canyon head is so incised into the shelf that reaches very close to the coastline, there is no physical space for this later refraction to take place. The curved refracted wave front reaches the coastline at a certain angle at both sides of the canyon axis, generating in turn new waves that move along the coast (Fig. 9). Two strong MWH peaks appear at both sides of the canyon projection for incisions exceeding 12 km, illustrating a 32% MWH increase with respect to a non-canyoned margin (Fig. 8). For an incision of 16 km the MWH is 3.3 m. These peaks reflect the positive interference of the secondary incident tsunami waves with these edge waves resulting in wave heights exceeding those of the first arrival. The seaward exponential decay of these waves from the coast, their sinusoidal shape and their propagation along the coast allow interpreting them as trapped edge waves (Fig. 9). These waves move along the coast at a relatively slow speed and, depending on tsunami source location, can arrive hours later than the direct wave, considerably increasing tsunami hazard. This type of wave has been reported to contain twice the energy of non-trapped tsunami waves (González et al., 1995) and can occur during a long time (~one week) after the first arrival (Miller et al., 1962; Rabinovich et al., 2006). Note for example in Figure 9 how the reflected wave in a margin with a 2-km-incised canyon is

noticeably higher than that in a margin with a 16-km-incised canyon, indicating that a significant portion of energy remains along the coast.

Changes in canyon width affect more the distribution of increased and decreased MWH rather than their magnitude. This is shown in Figure 10 for a constant canyon incision of 10 km and a 90° orientation. For canyon width values increasing from 6 to 10 km a gradual MWH 30% decrease occurs shoreward of the canyon head while a gradual MWH 8% increase at both sides of the canyon takes place compared to a non-canyoned margin. Increases in canyon width beyond 10 km do not produce further changes in MWH but a gradual geographic separation of the enhanced MWH at both sides of the canyon, thus enlarging the area along the coast affected by the presence of the canyon. Higher canyon width values (e.g. 20 km) lead to a widening and slight smoothing of the wave trough caused by the canyon head (Fig. 10).

For constant width and length, changes in the orientation of the canyon cause strong variations in the wave height profiles along the shoreline. The area of decreased MWH is shifted alongshore from the location of the canyon head projection, becoming less pronounced the more oblique the orientation is. For a canyon normal to the coastline (i.e. a 90° orientation), the wave height profile displays a symmetrical shape at both sides of the canyon head, whereas the more oblique the canyon is, the greater the asymmetry of the wave height distribution. This is imaged in Figure 11 for a 14 km wide, 10 km shelf incised canyon with orientations from 90° to 60° at 10° intervals. For oblique canyons, a greater wave build-up is produced along the canyon flank oriented towards the open ocean (i.e. the external canyon flank), whereas in the internal flank the MWH higher values decrease progressively and converge towards those of a non-canyoned margin (Fig. 11). This greater wave build-up is produced by the sum of the faster along-canyon oblique advancing front and the slower adjacent shelf front delayed by shoaling, that finally meet on the coast. These waves move along the coast at a relatively slow speed and, depending on tsunami source location, can arrive hours later than the

direct wave, considerably increasing tsunami hazard. The asymmetric distribution of MHW produced by canyon obliquity amplifies the effects of canyon incision and width.

For a 60°-oriented oblique canyon with a constant incision of 10 km (Fig. 12), the increase and decrease of higher and lower MWH values with augmenting canyon width remains similar to that described for a 90°-oriented canyon (Fig. 10). Wave set up in the external flank of the canyon generates higher MWH in longer stretches along the coast, whereas the reduction in the internal flank is evident too (Fig. 12).

Canyon obliquity has also significant effects when considering changes in the incision length for a constant canyon width of 14 km (Fig. 13). For a 60°-oriented oblique canyon, long shelf penetrating incisions lead to an enhanced asymmetry with increases of up to 35% in MWH in the external flank of the canyon with respect to a non-canyoned margin. The scenarios with the two largest incision lengths also result in the generation of edge waves, although the interference between them and the primary tsunami wave occurs at different locations than in a 90°-oriented canyon. For example, for a 16 km incision, one of these interferences produces a peak within the domain of lower MWH shoreward of the canyon head (Fig. 13).

From the above-described results it becomes clear that in terms of tsunami risk analysis, the presence of a submarine canyon incised into the continental shelf originates a greater variability in wave height and associated potential run-up along the adjacent coastline. In general, the synthetic scenarios here considered, with a deeply incised oblique canyon, generate worst-cases for certain locations along the coastline, with enhanced run-up potential, especially with the arrival of tsunami waves with negative sign.

### **3.3. The Blanes Canyon groundtruthing site**

The actual bathymetry of the Blanes margin, which is deeply incised by a canyon with the same name, and a second bathymetry where the canyon has been removed by simply connecting off-canyon depth contours, were used to simulate two tsunami scenarios using a positive, 0.5 m high and 20 min period incident wave. Figure 14 shows the MWH for the actual bathymetry (Fig. 14A) and for the non-canyoned bathymetry (Fig. 14B). The changes due to the presence of the Blanes Canyon with respect to other local effects in tsunami propagation are highlighted by the MWH numerical subtraction between both simulations (Fig. 14C). The results obtained are in agreement with those resulting from the previously presented theoretical scenarios. The main modification derived from the canyon incision occurs right shoreward of its head, where lower MWH values are found, and also up shore and down shore, where MWH values increase.

The canyon bathymetric anomaly reduces wave height by more than 2 m at the coast shoreward of its head, which represents half the height reached in the same margin with no canyon. The wave amplification effect up shore and down shore of the canyon head projection over the coast is also confirmed, with waves up to 50% higher than if no canyon was present. Also the obliquity effect of the Blanes Canyon results in higher MWH face to the ocean looking external flank of the canyon to the north (Fig. 14C).

Observations on the location of MWH during some historical tsunamis fit with our theoretical results. In the Barisal margin, in Bangladesh, the submarine canyon cut into the shelf is oriented northeast and during the 2004 Indian Ocean tsunami the MWH was found shoreward of the eastern flank of the canyon head (Ioualalen et al., 2007), exactly as predicted in our Figures 12 and 13. In Sissano Lagoon, where the canyon is normal to the coastline direction, the MWH was recorded shoreward of both flanks of the canyon head (Matsuyama et al., 1999; Tappin et al., 2001), as also shown in our Figures 8 and 10.

The ground truth exercise using the actual bathymetry of the Blanes Canyon area, together with the evidence provided by the above-mentioned historical events, confirm the relevance of submarine canyons for tsunami propagation and impact along the nearby coast by significantly modifying the final wave height and run-up. To that point, the Blanes Canyon area could be considered representative of a large number of submarine canyon settings in the world ocean (Harris and Whiteway, 2011).

#### **4. Concluding remarks**

The presence of a submarine canyon modifies tsunami wave arrival time and height along the adjacent coast. In general, tsunami arrival time to the coastal stretch located shoreward of the canyon head is shortened due to the lowered shoaling effect because of the greater water depth of the canyon itself. In contrast, both parameters increase up and down coast, also due to the bathymetric anomaly the canyon represents. MWH is modified by submarine canyons in two main ways: (1) by preventing wave set up along their axis, which leads to lowered MWH shoreward of the canyon head in comparison to non-canyoned margins, and (2) by enhancing wave set up along and over both flanks of the canyon head, thus producing relatively higher MWH sideward. Wave height and arrival time variations are larger when the sign of the incident wave is negative (i.e. when the trough arrives first). The following relations between canyon geomorphic parameters and arrival time and wave height have been identified:

(1) The more shelf incised a canyon is (i.e. the closer the canyon head to the coastline), the larger their effects are on MWH and arrival times. Extremely incised canyons favour the formation of trapped edge waves.

(2) Canyon width influences the extension of decreased and increased MWH and shorter arrival times to specific locations.

(3) Canyon orientation controls the distribution of MWH reaching the coast, producing asymmetric distributions with larger MWH and longer arrival times shoreward of the ocean looking flank of the canyon head.

Tsunami simulations performed in the Blanes Canyon, in the North Catalan margin, demonstrate that the general relations observed in the theoretical scenarios are applicable to actual continental margin configurations, and that the effects produced by the canyon are at least of equal magnitude than other coastal effects.

This study aims at understanding the general behaviour of tsunami waves when travelling over submarine canyons with their heads close to the shoreline, and how canyon geomorphic characteristics modify the tsunami wave. The results obtained could be applied to identify tsunami flood-prone coastal stretches within a given area, thus helping to improve prevention, mitigation and evacuation strategies in case of tsunami occurrence. This study also highlights the benefits of high-resolution bathymetric data at considerable depths beyond the shallow continental shelf in tsunami-prone areas.

### **Acknowledgements**

This research was supported by the ASTARTE RTD project funded by the European Commission Seventh Framework Program, the GRACCIE-CONSOLIDER project (ref. CSD2007-00067) of the Spanish RTD Program, and Generalitat de Catalunya “Grups de Recerca Consolidats” grant 2009 SGR 1305. The Blanes Canyon bathymetry was obtained in the frame of PROMETEO (ref. CTM2007-66316-C02-01/MAR) and DOS MARES (ref. CTM2010-21810-C03-01/MAR) Spanish research projects. O. Iglesias was supported by a FPU fellowship of the Spanish Ministry of Education. We thank C. Mueller, an anonymous reviewer and the editor for their thoughtful revisions. We also thank Philip Liu’s Research Group of Cornell University for making available the COMCOT software in its web page. The

528 publication reflects only the views of the authors. The EC is not liable for any use that may be made  
529 of the information contained in this article.  
530



531     **References**

- 532     Amblas, D., Canals, M., Urgeles, R., Lastras, G., Liqueste, C., Hughes-Clarke, J.E., Casamor, J.L., Calafat,  
533     A.M., 2006. Morphogenetic mesoscale analysis of the northeastern Iberian margin, NW  
534     Mediterranean Basin. *Marine Geology* 234 (1-4): 3-20.
- 535     Amblas, D., Gerber, T.P., De Mol, B., Urgeles, R., Garcia-Castellanos, D., Canals, M., Pratson, L.F., Robb,  
536     N., Canning, J., 2012. Survival of a submarine canyon during long-term outbuilding of a continental  
537     margin. *Geology* 40: 543-546.
- 538     Allen, S.E., 2000. On subinertial flow in submarine canyons: effect of geometry. *Journal of*  
539     *Geophysical Research* 105 (C1): 1285-1297.
- 540     Allen, S.E., Hickey, B.M., 2010. Dynamics of advection-driven upwelling over a shelf break submarine  
541     canyon. *Journal of Geophysical Research* 115 (C8): C08018.
- 542     Bates, R.L. Jackson, J.A., 1980. *Glossary of Geology*. American Geological Institute, Falls Church, 751  
543     pp.
- 544     Canals, M., Casamor, J.L., Urgeles, R., Farrán, M., Calafat, A.M., Amblas, D., Willmott, V., Estrada, F.,  
545     Sánchez, A., Arnau, P.J., Colás, S., 2004. Mapa del relleu submarí de Catalunya (Seafloor relief map of  
546     Catalonia), 1:250 000. Institut Cartogràfic de Catalunya, Barcelona, Spain, 1 map.
- 547     Canals, M., Puig, P., Heussner, S., Durrieu de Madron, X., Palanques, A., Fabres, J., 2006. Flushing  
548     submarine canyons. *Nature* 444: 354-357.
- 549     Clark, J.D., Pickering, K.T., 1966. *Submarine channels: processes and architecture*. Vallis, London, 231  
550     pp.
- 551     Covault, J.A., Fildani, A., Romans, B.W., McHargue, T. 2011. The natural range of submarine canyon-  
552     and-channel longitudinal profiles. *Geosphere* 7 (2): 313-332.
- 553     Cutchin, D.L., Smith R.L., 1973. Continental shelf waves: Low-frequency variation in sea level and  
554     currents over the Oregon continental shelf. *Journal of Physical Oceanography* 3: 73-82.

555 Daly, R.A., 1936. Origin of submarine canyons. *American Journal of Science* 31: 401-420.

556 Divyalakshmi, K.S., Rammohan, V., Ramana Murthy, M.V., 2011. Modification of tsunami wave by  
557 submarine canyon: Case Study of Multiple Canyons at South East Coast of India. *Marine Geodesy* 34:  
558 2-15.

559 Gica, E., Spillane, M.C., Titov, V.V., Chamberlin, C., Newman, J.C., 2008. Development of the forecast  
560 propagation database for NOAA's Short-term Inundation Forecast for Tsunamis (SIFT). NOAA Tech.  
561 Memo. OAR PMEL-139, 89 pp.

562 González, F.I., Satake, K., Boss, E.F., Mofjeld, H.O., 1995. Edge wave and non-trapped modes of the 25  
563 April 1992 Cape Mendocino tsunami. *Pure and Applied Geophysics* 144 (3-4): 409-426.

564 Harris, P.T., Whiteway, T., 2011. Global distribution of large submarine canyons: Geomorphic  
565 differences between active and passive continental margins. *Marine Geology* 285: 69-86.

566 Inman, D.L., 1953. Areal and seasonal variations in beach and nearshore sediment at La Jolla,  
567 California. Technical Memorandum no. 39, Beach Erosion Board Corps of Engineers, Department of  
568 the Army, USA, pp. 82 and appendices.

569 Ioualalen, M., Pelinovsky, E., Asavanant, J., Lipikorn, R., Descamps, A., 2007. On the weak impact of  
570 the 26 December Indian Ocean tsunami on the Bangladesh coast. *Natural Hazards and Earth System*  
571 *Sciences* 7: 141-147.

572 Jobe, Z.R., Lowe, D.R., Uchytel, S.J., 2011. Two fundamentally different types of submarine canyons  
573 along the continental margin of Equatorial Guinea. *Marine and Petroleum Geology* 28 (3): 843-860.

574 Klinck, J.M., 1989. Geostrophic adjustment over submarine canyons. *Journal of Geophysical*  
575 *Research* 94 (C5): 6133-6144.

576 Lastras, G., Acosta, J., Muñoz, A., Canals, M., 2011. Submarine canyon formation and evolution in the  
577 Argentine Continental Margin between 44°30'S and 48°S. *Geomorphology*, 128: 116-136.

578 Lastras, G., Canals, M., Amblas, D., Lavoie, C., Church, I., De Mol, B., Duran, R., Calafat, A.M., Hughes-  
579 Clarke, J.E., Smith, C.J, Heussner, S., “Euroleón” cruise shipboard party, 2011. Understanding sediment  
580 dynamics of two large submarine valleys from seafloor data: Blanes and La Fonera canyons,  
581 northwestern Mediterranean Sea. *Marine Geology*, 280 (1–4): 20-39.

582 Li, L., Qiu, Q., Huang, Z., 2012. Numerical modeling of the morphological change in Lhok Nga, west  
583 Banda Aceh, during the 2004 Indian Ocean tsunami: understanding tsunami deposits using a forward  
584 modeling method. *Natural Hazards* 64: 1549-1574.

585 Lipa, B., Barrick, D., Saitoh, S.I., Ishikawa, Y., Awaji, T., Largier, J., Garfield, N., 2011. Japan Tsunami  
586 Current Flows Observed by HF Radars on Two Continents. *Remote Sensing* 3: 1663-1679.

587 Matsuyama, M., Walsh, J.P., Yeh, H., 1999. The effect of bathymetry on tsunami characteristics at  
588 Sisano Lagoon, Papua Guinea. *Geophysical Research Letters* 26 (23): 3513-3516.

589 Merrifield, M.A., Firing, Y. L. Firing, Y. L. Agricole, W. Brundrit, G., Chang-Seng, D., Farre, R., Kilonsky,  
590 B., Knight, W., Kong, L., Magori, C., Manurung, P., McCreery, C., Mitchell, W., Pillay, S., Schindele, F.,  
591 Shillington, F., Testut, L., Wijeratne, E.M.S., Caldwell, P., Jardin, J., Nakahara, S., Porter, F.-Y., Turetsky,  
592 N., 2005. Tide gauge observations of the Indian Ocean tsunami, December 26, 2004. *Geophysical*  
593 *Research Letters* 32 (9): 1944-8007.

594 Miller, G.R., Munk, W.H., Snodgrass, F.E., 1962. Long-period waves over California’s continental  
595 borderland. Part II. Tsunamis. *Journal of Marine Research* 20 (1): 31-41.

596 NOAA (National Oceanic and Atmospheric Administration), 2012a. Natural Hazard Viewer  
597 (<http://maps.ngdc.noaa.gov/viewers/hazards/?layers=0>).

598 NOAA (National Oceanic and Atmospheric Administration), 2012b. 1-Minute Water Level Data. Center  
599 for Operational Oceanographic Products and Services, Tsunami Capable Tide Stations.  
600 (<http://tidesandcurrents.noaa.gov/1mindata.shtml>).

601 Normark, W.R., Piper, D.J.W., 1969. Deep-sea fan-valleys, past and present. Geological Society of  
602 America Bulletin 80: 1859-1866.

603 Pirmez, C., Beauboeuf, R.T., Friedmann, S.J., Mohrig, D.C., 2000. Equilibrium profile and baselevel in  
604 submarine channels: examples from Late Pleistocene systems and implications for the architecture of  
605 deepwater reservoirs. Gulf Coast Section Society of Economic Paleontologists and Mineralogists  
606 Foundation 20th Annual Research Conference, Houston, pp. 782-805.

607 Rabinovich, A.B., 2009. Seiches and harbour oscillations. Handbook of Coastal and Ocean  
608 Engineering. World Scientific Publishing Company, Singapore, pp. 193-236.

609 Rabinovich, A.B., Stephenson, F.E., Thomson, R.E., 2006. The California Tsunami of 15 June 2005 along  
610 the coast of North America. Atmosphere-Ocean 44 (4): 415-427.

611 Sahal, A., Roger, J., Allgeyer, S., Lemaire, B., Hébert, H., Schindele, F., Lavigne, F., 2009. The tsunami  
612 triggered by the 21 May 2003 Boumerdès-Zemmouri (Algeria) earthquake: field investigations on the  
613 French Mediterranean coast and tsunami modelling. Natural Hazards and Earth System Sciences 9:  
614 1823-1834.

615 Shepard, F.P., Dill, R.F., 1966. Submarine Canyons and Other Sea Valleys. Rand McNally, Chicago, 381  
616 pp.

617 Takeda, H., 1984. Topographically Trapped Waves over the Continental Shelf and Slope. Journal of the  
618 Oceanographical Society of Japan 40: 349-366.

619 Tang, L., Titov, V.V., Chamberlin, C.D., 2009. Development, testing, and applications of site-specific  
620 tsunami inundation models for real-time forecasting. Journal of Geophysical Research 114 (C12):  
621 C12025.

622 Tappin, D.R., Watts, P., McMurtry, G.M., Lafoy, Y., Matsumoto, T., 2001. The Sissano, Papua New  
623 Guinea tsunami of July 1998 — Offshore evidence on the source mechanism. Marine Geology, 175  
624 (1–4): 1-23.

625 van den Hove, S., Moreau, V., 2007. Deep-Sea Biodiversity and Ecosystems: A scoping report on their  
 626 socio-economy, management and governance. Biodiversity Series 28. UNEP-WCMC, HERMES project,  
 627 Cambridge, 84 pp.

628 Wåhlin, A.K., 2002. Topographic steering of dense currents with application to submarine canyons.  
 629 Deep Sea Research 49 (Part II): 305-320.

630 Wang, X., 2009. User manual for COMCOT version 1.7 (first draft). [http://ceeserver.cee.cornell.edu/](http://ceeserver.cee.cornell.edu/pll-group/comcot.htm)  
 631 [pll-group/comcot.htm](http://ceeserver.cee.cornell.edu/pll-group/comcot.htm)

632 Ward, S. N., 1989. Tsunamis, Encyclopedia of Solid Earth Geophysics, Van Nostrand Reinhold  
 633 company, New York, 13 pp.

634 Wu, T.R., Chen, P.F., Tsai, W.T., Chen, G.Y., 2008. Numerical Study on Tsunamis Excited by 2006 Pintung  
 635 Earthquake Doublet. Terrestrial, Atmospheric and Oceanic Sciences 19 (6): 705-715.

636 Yamazaki, Y., Cheung, K.F., 2011. Shelf resonance and impact of near-field tsunami generated by the  
 637 2010 Chile earthquake. Geophysical Research Letters 38 (12): L12605.

638

## Figure Captions

**Fig. 1.** Example of one of the synthetic surfaces used in this study, corresponding to a submarine canyon with an incision length of 14 km, a width of 20 km and orientation of 70° with respect to the surrounding depth contours and margin orientation. The location of the origin of coordinates and the extension of the study area are depicted. Additional areal extension sideward of the central study area in the y direction has been used in the simulations to prevent edge effects but is not displayed in the following figures.

**Fig. 2.** Canyon geomorphic parameters taken into account in this study.

**Fig. 3.** Time profiles of the synthetic incident tsunami waves used in this study.

**Fig. 4.** A: Maximum wave height distribution of the four control tsunami scenarios run over a non-canyoned margin, with a positive wave amplitude of 0.5 m and periods of 20, 30, 40 and 50 min. Note that at short distance to the coastline and over the slope, tsunami waves are higher than in the continental shelf and the deep basin, except for a period of 20 min. B: Power spectral density using Fast Fourier Transform calculated with a 1-min time step and a time interval of 90 min for a synthetic station located at the coastline, for each of the periods computed.

**Fig. 5.** Products obtained for each of the 514 scenarios, exemplified for a 20 km wide and 16 km incised canyon, oriented 60° with respect to the shelf edge and an incident positive wave of 20 min period and 0.5 m high. A: Maximum wave heights plot. White points along the simulated coastline correspond to the location of 21 synthetic tide gauges, and the white region to region represents emerged land. B: Synthetic marigrams from tide gauges 12, 15 and 18 (see location in A). C: Wave height distribution at 19, 29 and 41 min time steps. Black lines in A and C represent isobaths every 100 m.

**Fig. 6.** Arrival time of the first positive peak at each of the 21 tide gauges (see location in Fig. 5A) for each of the 514 scenarios considered. Significant tsunami arrival time dependence from the analysed canyon and wave parameters can be observed. See main text for further explanation.

**Fig. 7.** Maximum wave height along the 10 m isobath at a constant distance of 100 m from the coastline produced by a positive, 0.5 m amplitude, 20 min period tsunami wave, for each of the 514 scenarios considered. See main text for further explanation.

**Fig. 8.** Maximum wave height along the 10 m isobath at a constant distance of 100 m from the coastline produced by a positive, 0.5 m amplitude, 20 min period tsunami in a non-canyoned margin (left stripe) and in a margin incised by a 14 km wide, 90° oriented canyon with incision lengths from 2 to 16 km. Highest and lowest maximum wave heights for each configuration are displayed in the bottom panel.

**Fig. 9.** Wave height distribution at 20, 40 and 60 min observed during the simulation of a positive, 0.5 m amplitude, 20 min period tsunami in a margin carved by a 20 km wide, 90° oriented canyon. Top panels are for a 16 km incised canyon, whereas bottom panels are for a 2 km incised canyon. Dashed red lines depict the rounded shape of the wave front above the canyon head at 20 min, much more marked for the 16-km-incised canyon. Dashed black lines show the edge waves generated nearshore at 40 min (exponential profile) and displaced along the coast at both sides of the canyon at 60 min (sinusoidal in x-direction). These edge waves are only generated with the 16-km-incised canyon. Dashed blue lines show the location of the reflected wave at 60 min.

**Fig. 10.** Maximum wave height along the 10 m isobath at a constant distance of 100 m from the coastline produced by a positive, 0.5 m amplitude, 20 min period tsunami in a non-canyoned margin (left stripe) and in a margin carved by a 10 km incised, 90°-oriented canyon with widths from 6 to 20 km. Highest and lowest maximum wave heights for each configuration are displayed in the bottom panel.

**Fig. 11.** Maximum wave height along the 10 m isobath at a constant distance of 100 m from the coastline produced by a positive, 0.5 m amplitude, 20 min period tsunami in a non-canyoned margin (left stripe) and in a margin carved by a 10 km incised, 14 km wide canyon with orientations from 60° to 90° normal to the general depth contours. Highest and lowest maximum wave heights for each configuration are displayed in the bottom panel.

690 **Fig. 12.** Maximum wave height along the 10 m isobath at a constant distance of 100 m from the  
691 coastline produced by a positive, 0.5 m amplitude, 20 min period tsunami in a non-canyoned margin  
692 (left stripe) and in a margin carved by a 10 km incised, 60°-oriented canyon with widths from 6 to 20  
693 km. Highest and lowest maximum wave heights for each configuration are displayed in the bottom  
694 panel.

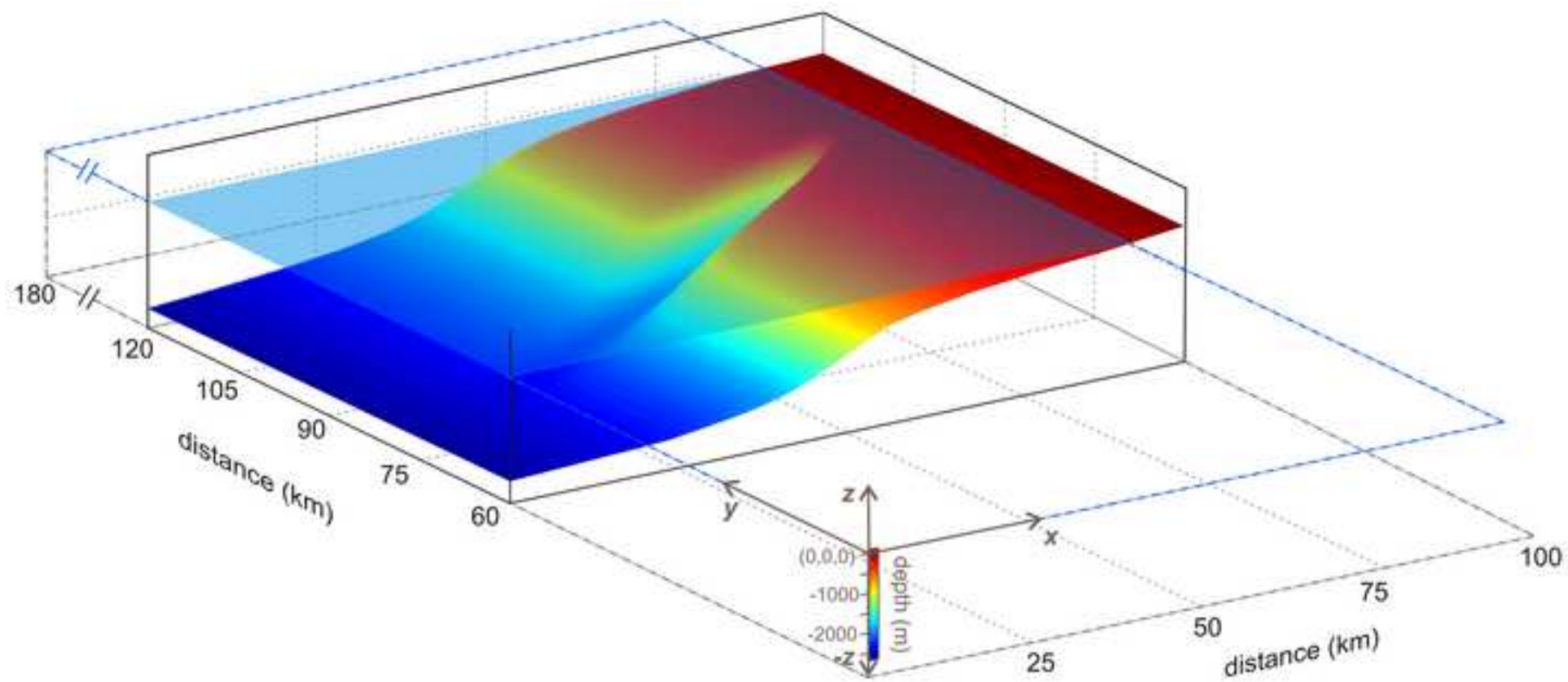
695 **Fig. 13.** Maximum wave height along the 10 m isobath at a constant distance of 100 m from the  
696 coastline produced by a positive, 0.5 m amplitude, 20 min period tsunami in a non-canyoned margin  
697 (left stripe) and in a margin carved by a 14 km wide, 60°-oriented canyon with incision lengths from 2  
698 to 16 km. Highest and lowest maximum wave heights for each configuration are displayed in the  
699 bottom panel.

700 **Fig. 14.** Effect of the propagation of a positive tsunami wave 0.5 m in amplitude and 20 min of period  
701 over the Blanes Canyon. A: Maximum wave height distribution over the actual bathymetry of the  
702 Blanes Canyon. B: Maximum wave height distribution over the bathymetry from where the canyon  
703 has been erased. C: Numerical subtraction between A and B. Black lines represent isobaths every 100  
704 m.

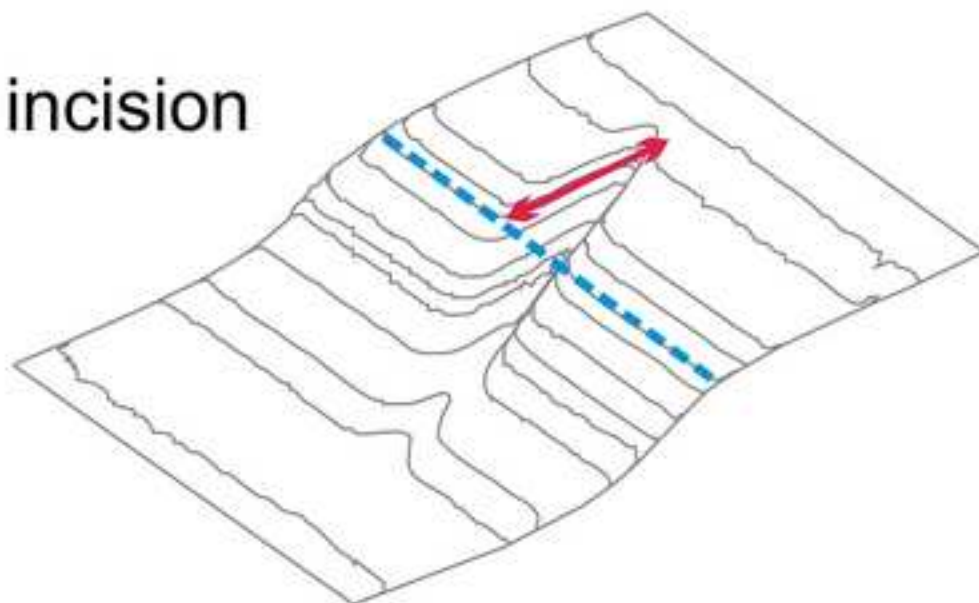


Figure1

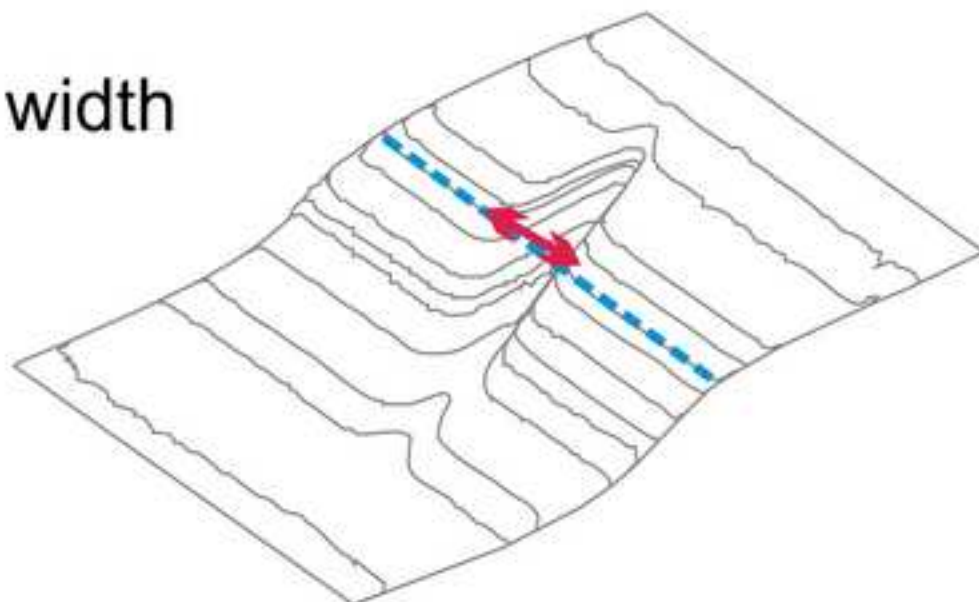
[Click here to download high resolution image](#)



incision



width



orientation

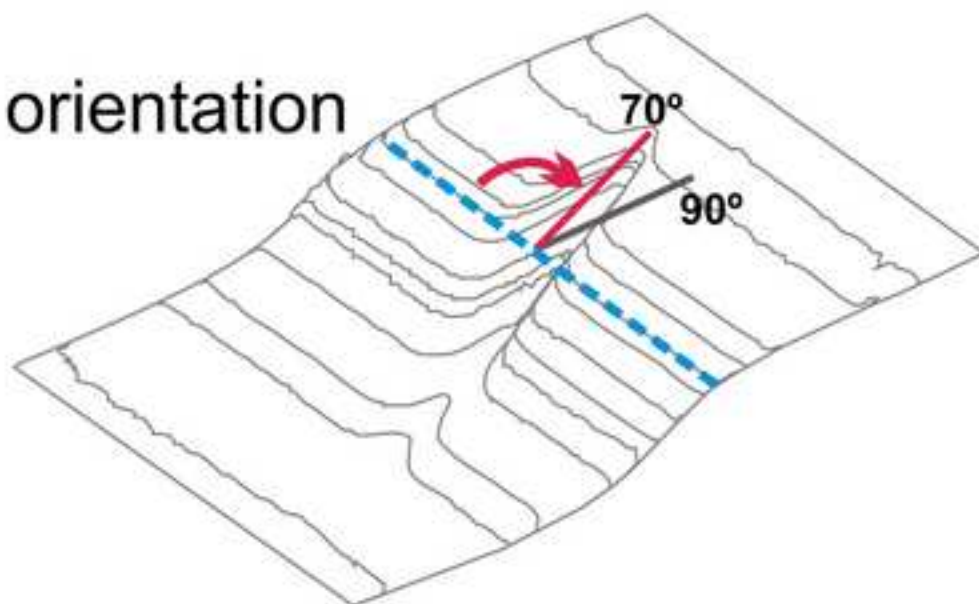


Figure3

[Click here to download high resolution image](#)

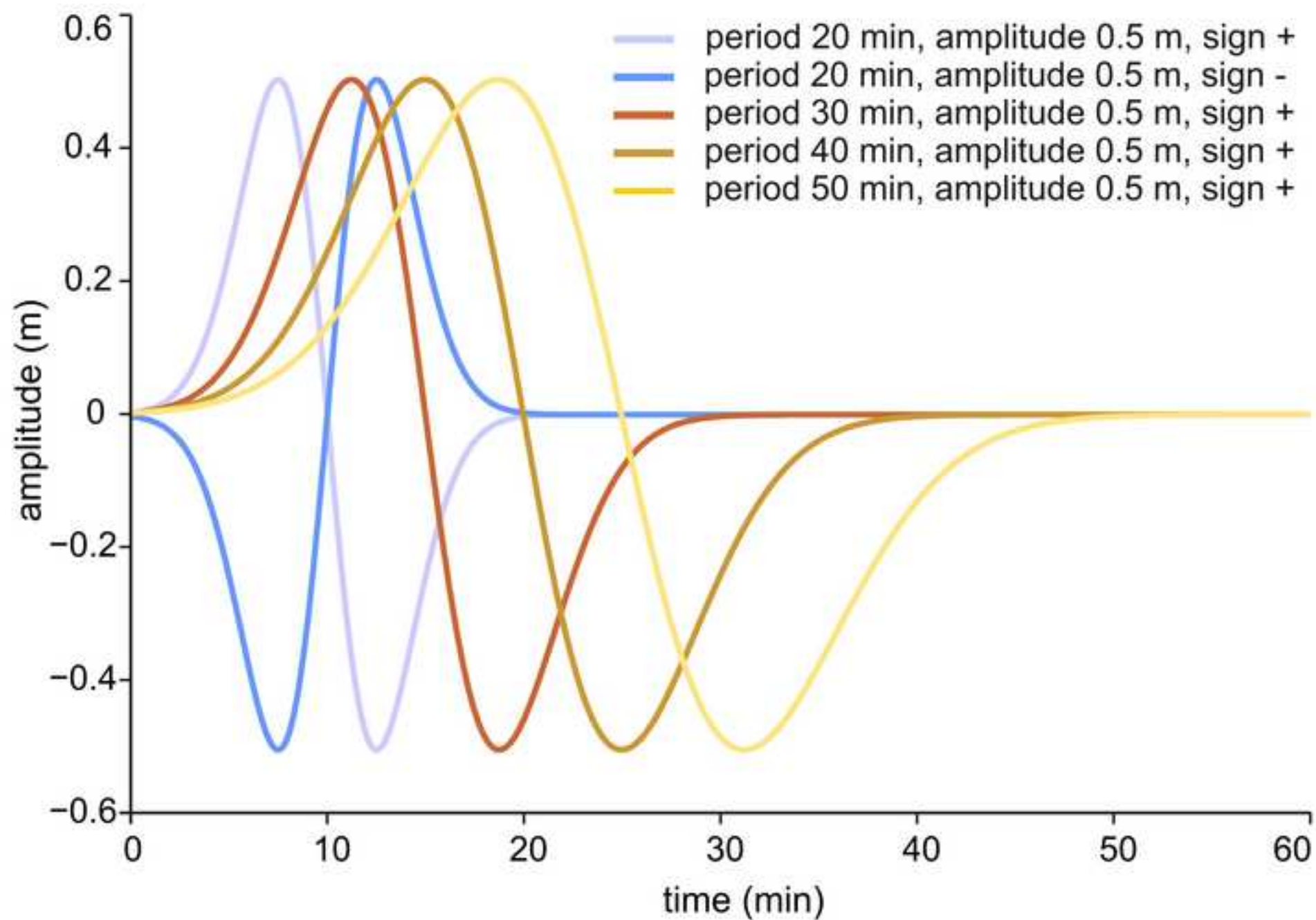


Figure4

[Click here to download high resolution image](#)

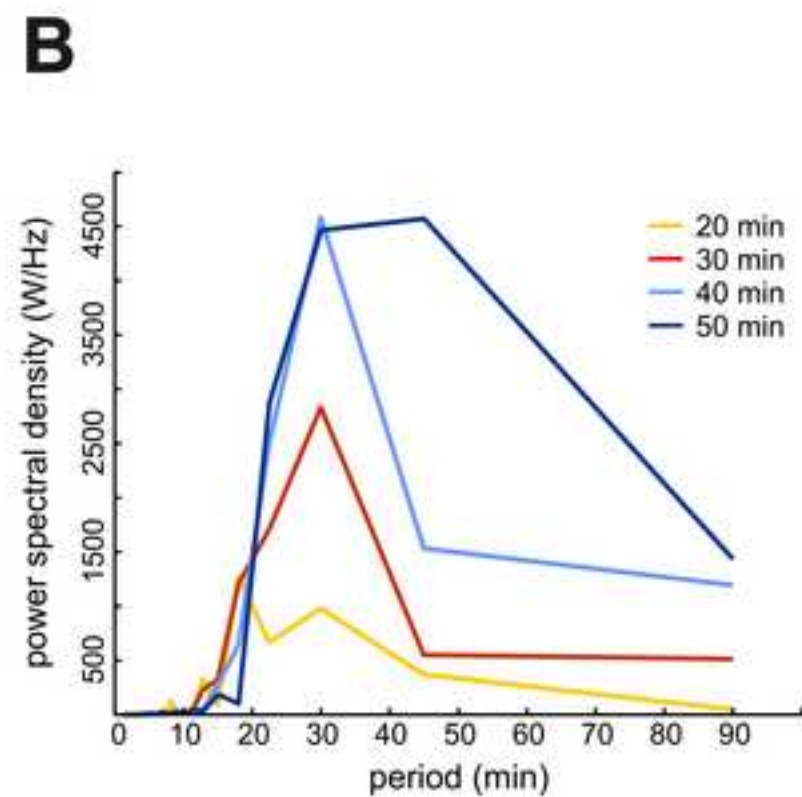
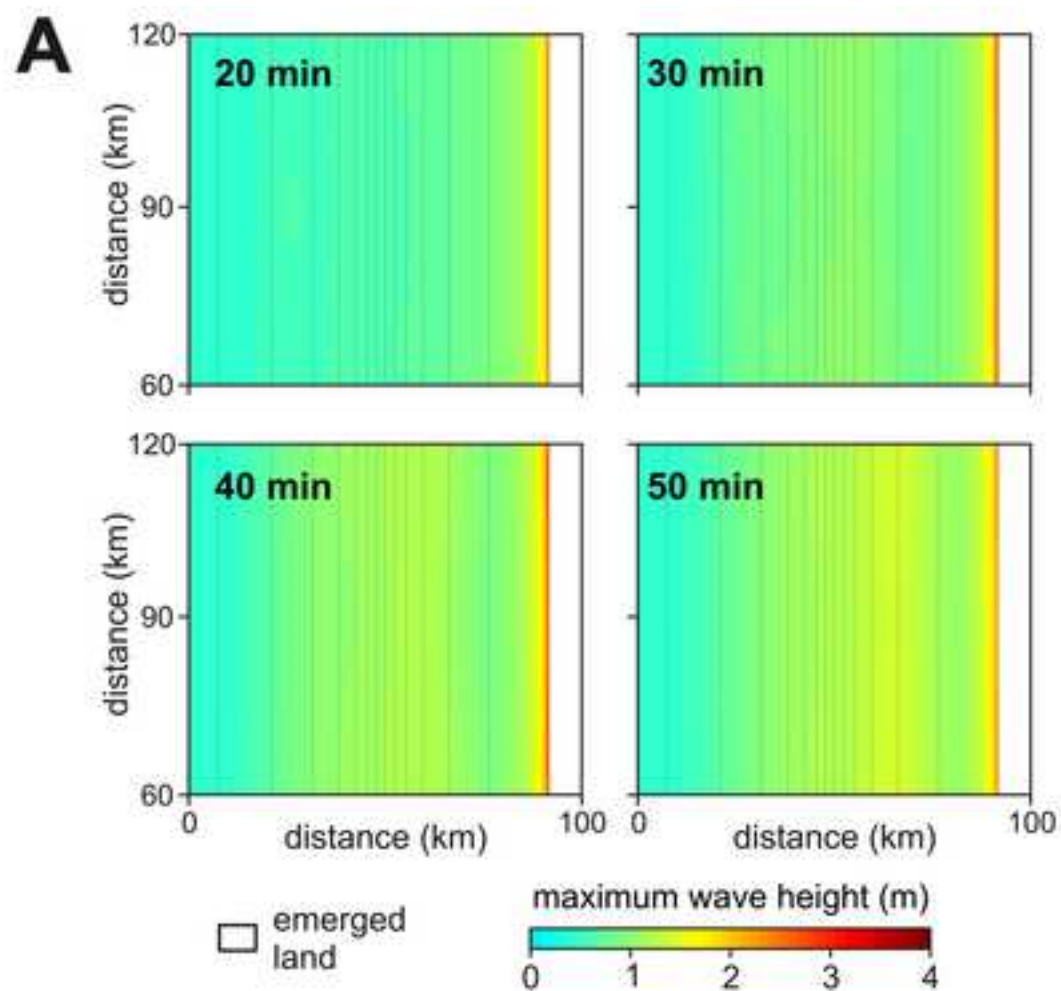
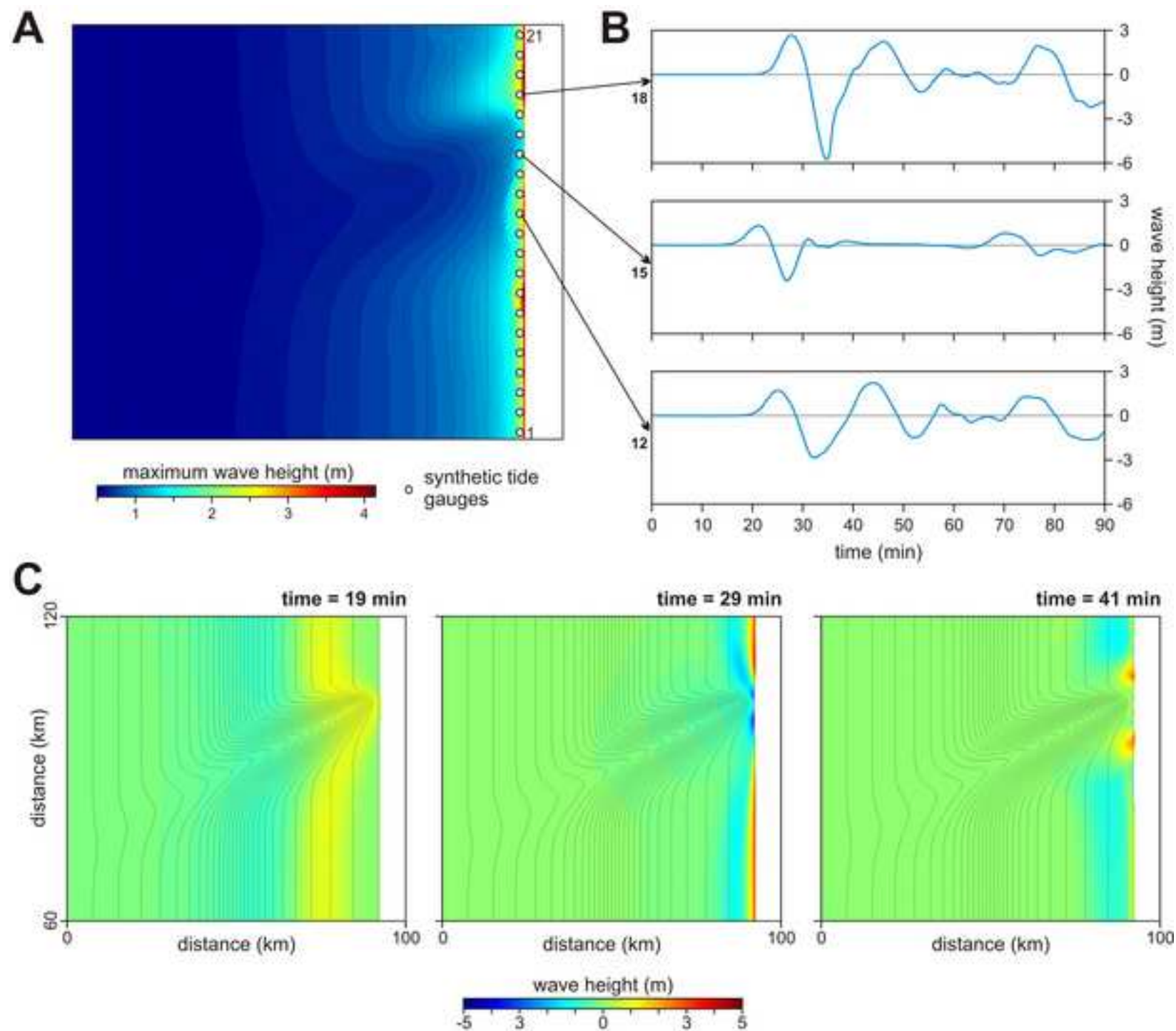


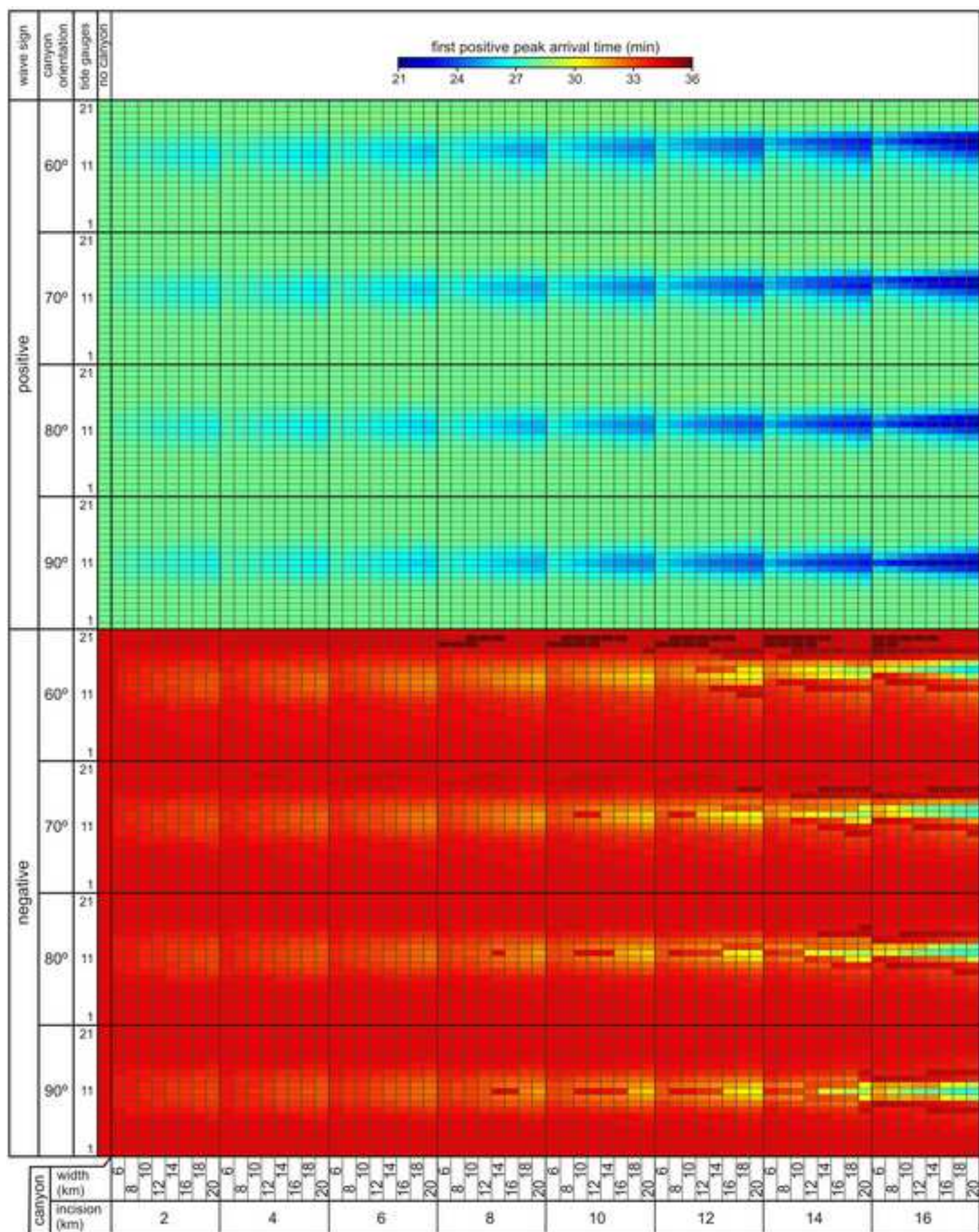
Figure5

[Click here to download high resolution image](#)





[Click here to download high resolution image](#)





[Click here to download high resolution image](#)

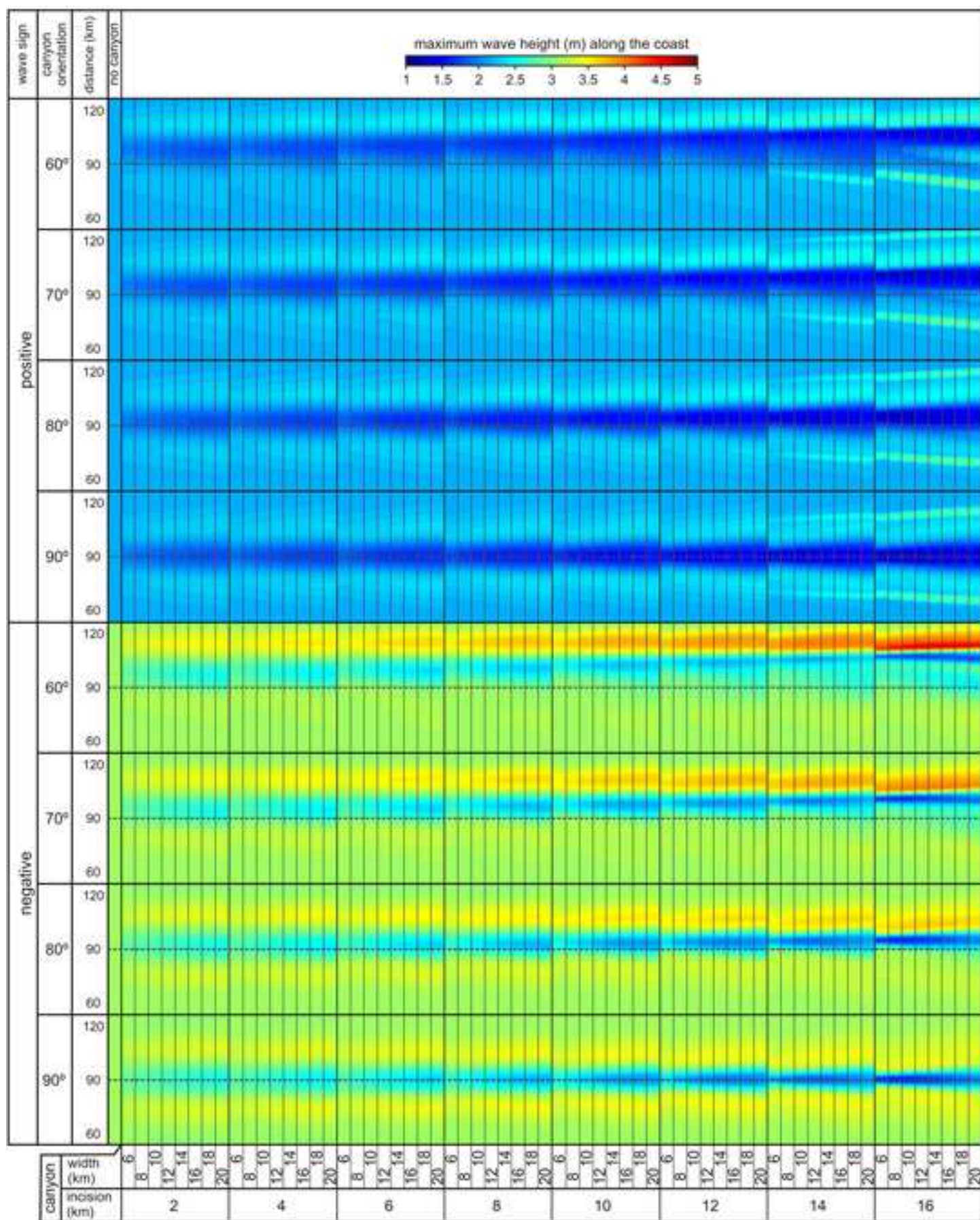


Figure8  
[Click here to download high resolution image](#)

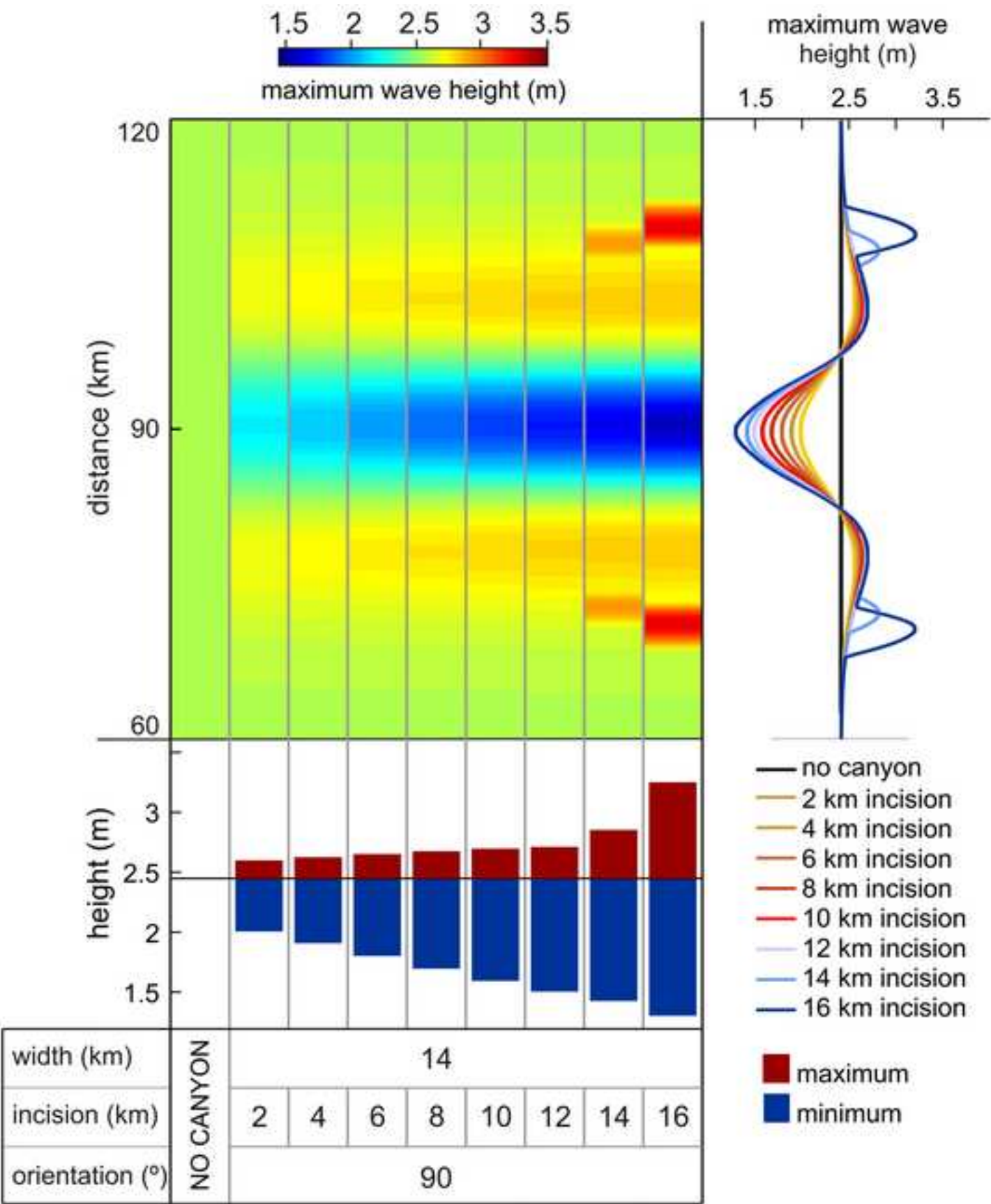




Figure9

[Click here to download high resolution image](#)

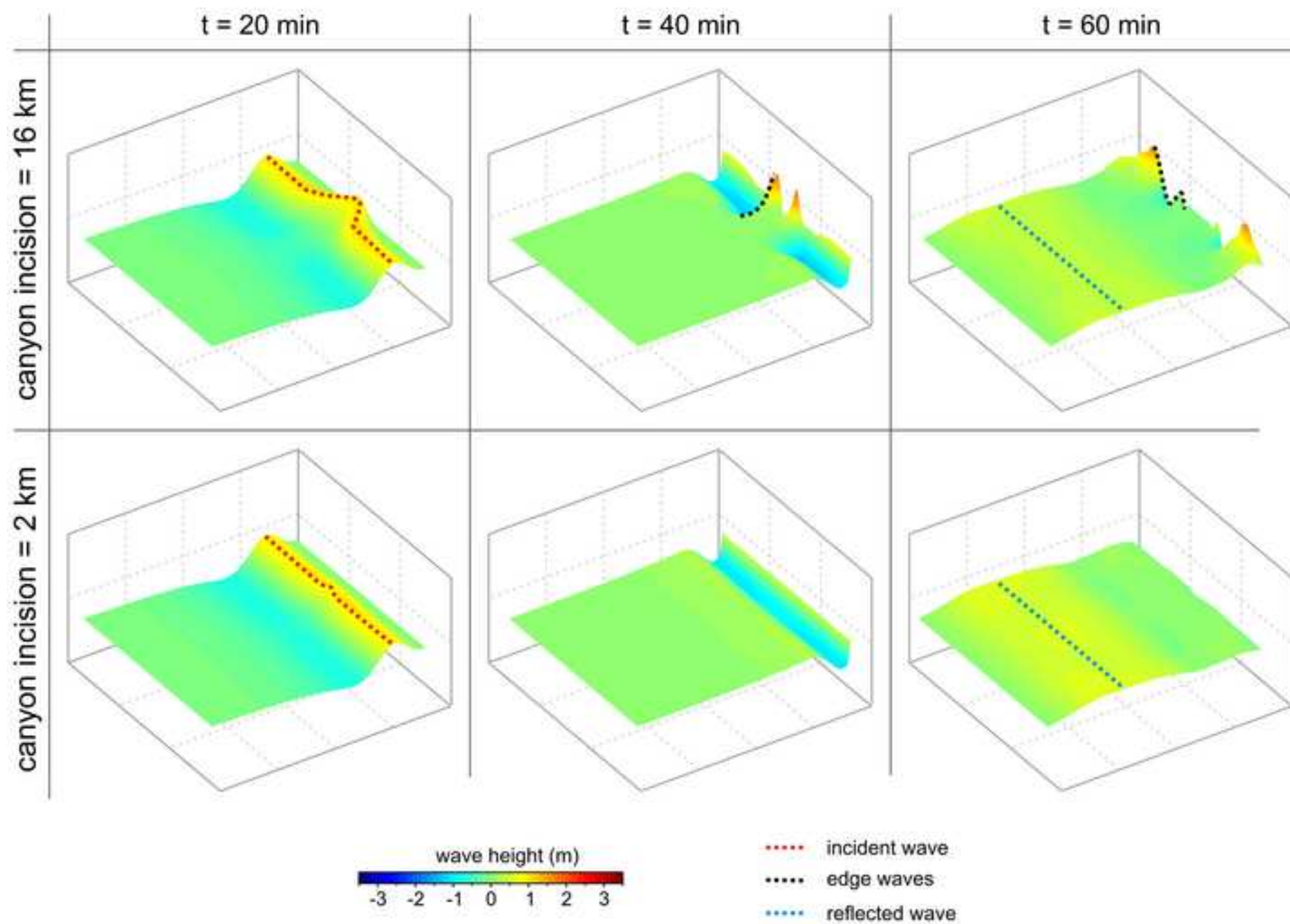


Figure10  
[Click here to download high resolution image](#)

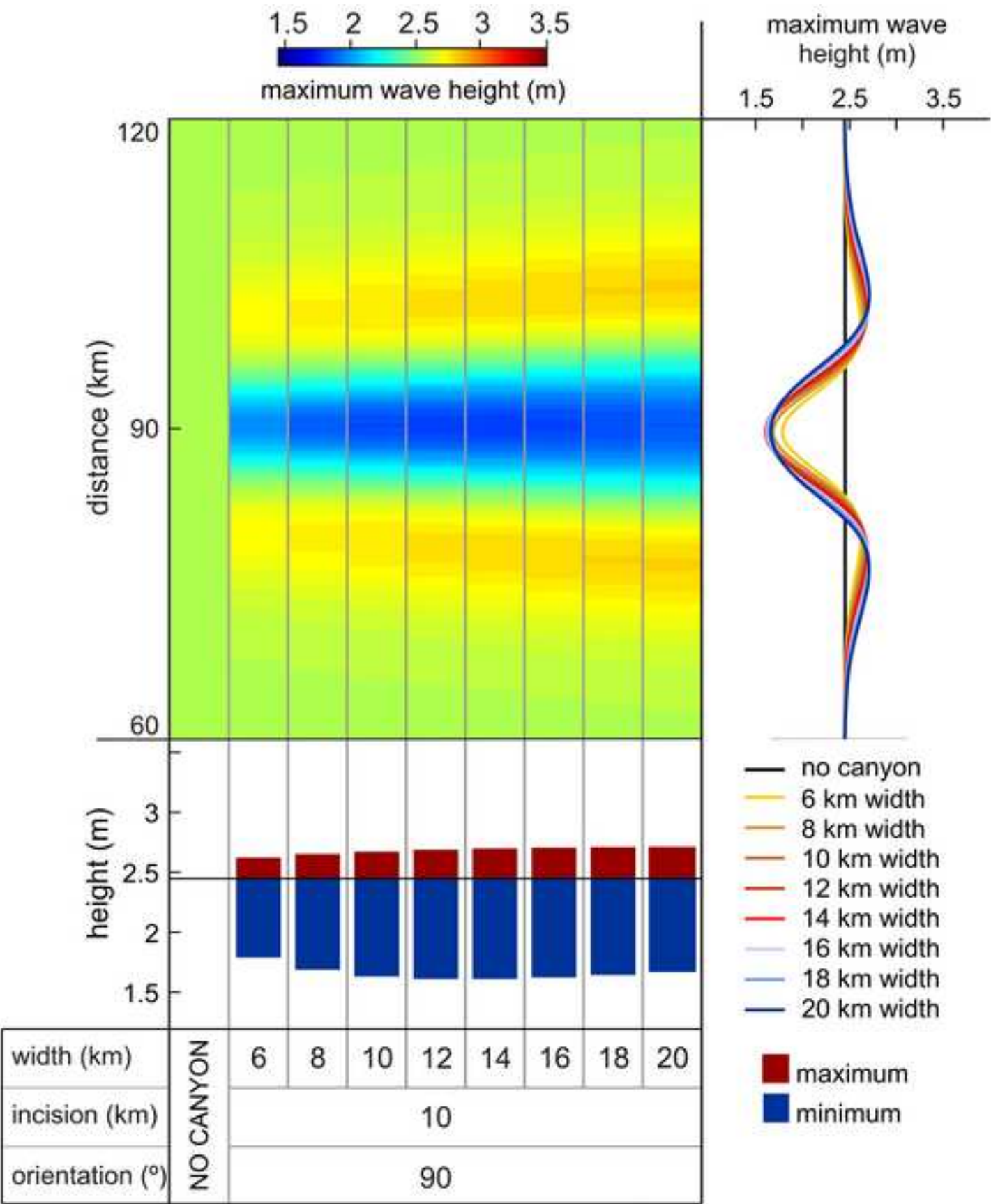


Figure11  
[Click here to download high resolution image](#)

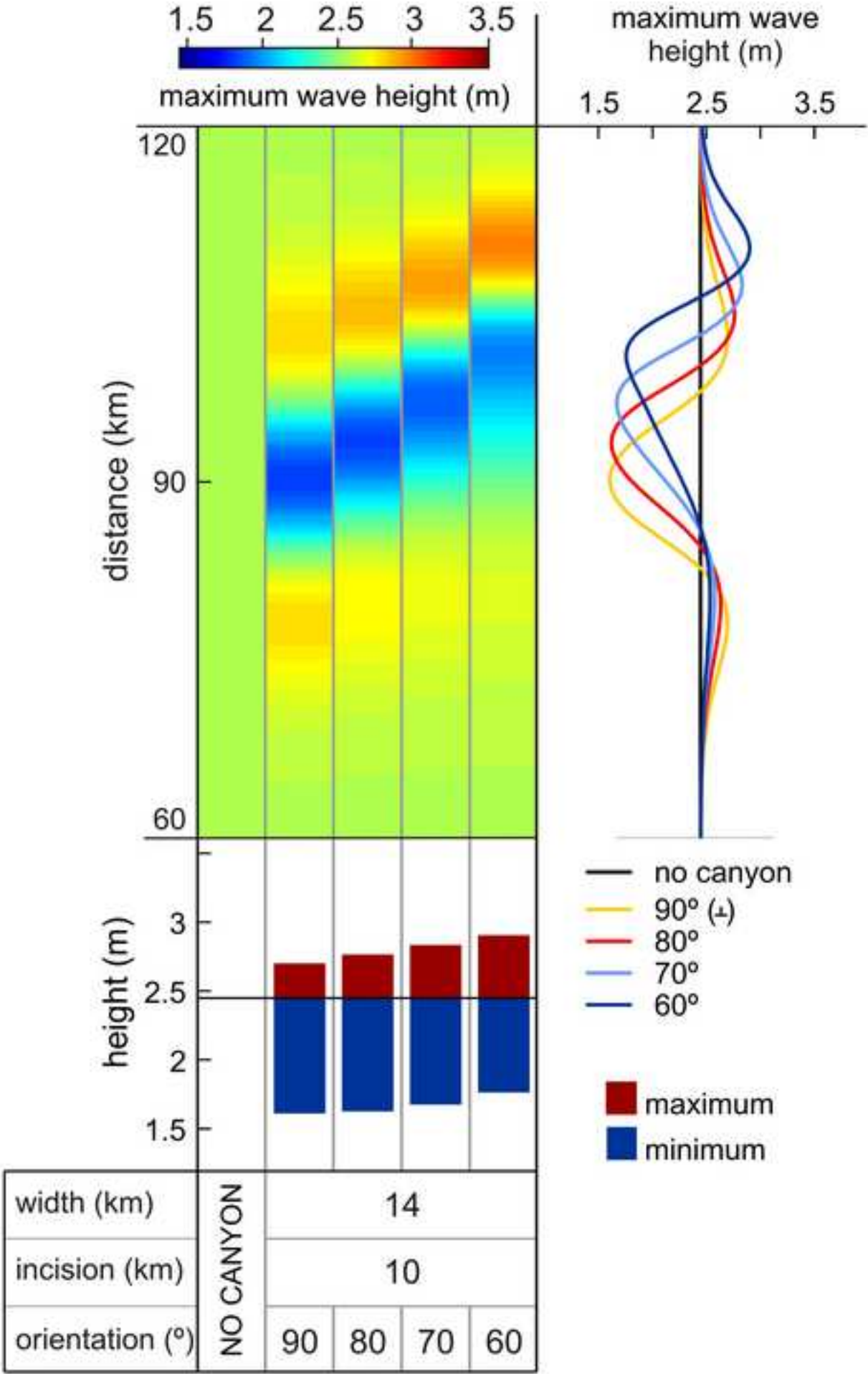


Figure12

[Click here to download high resolution image](#)

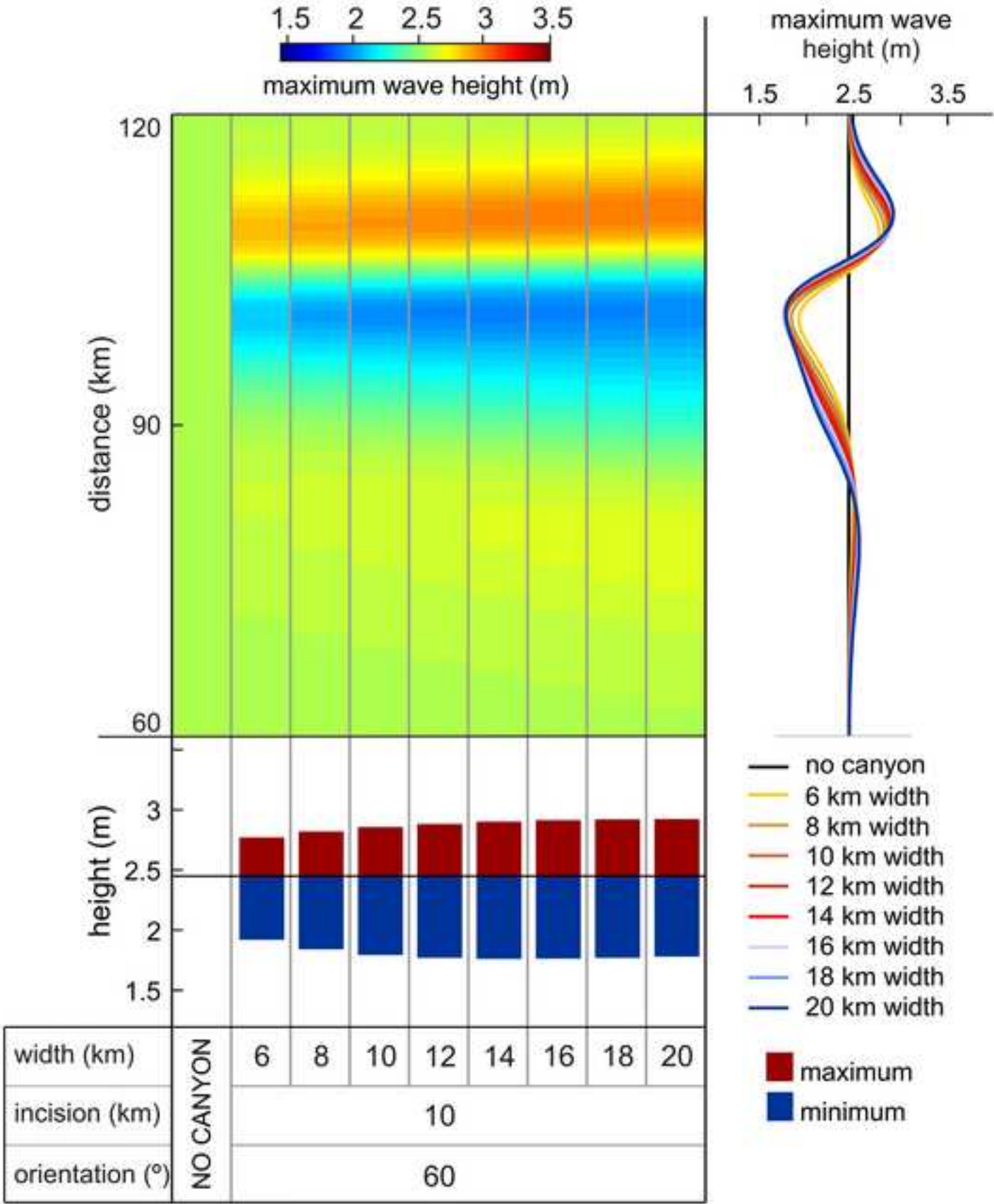




Figure13  
[Click here to download high resolution image](#)

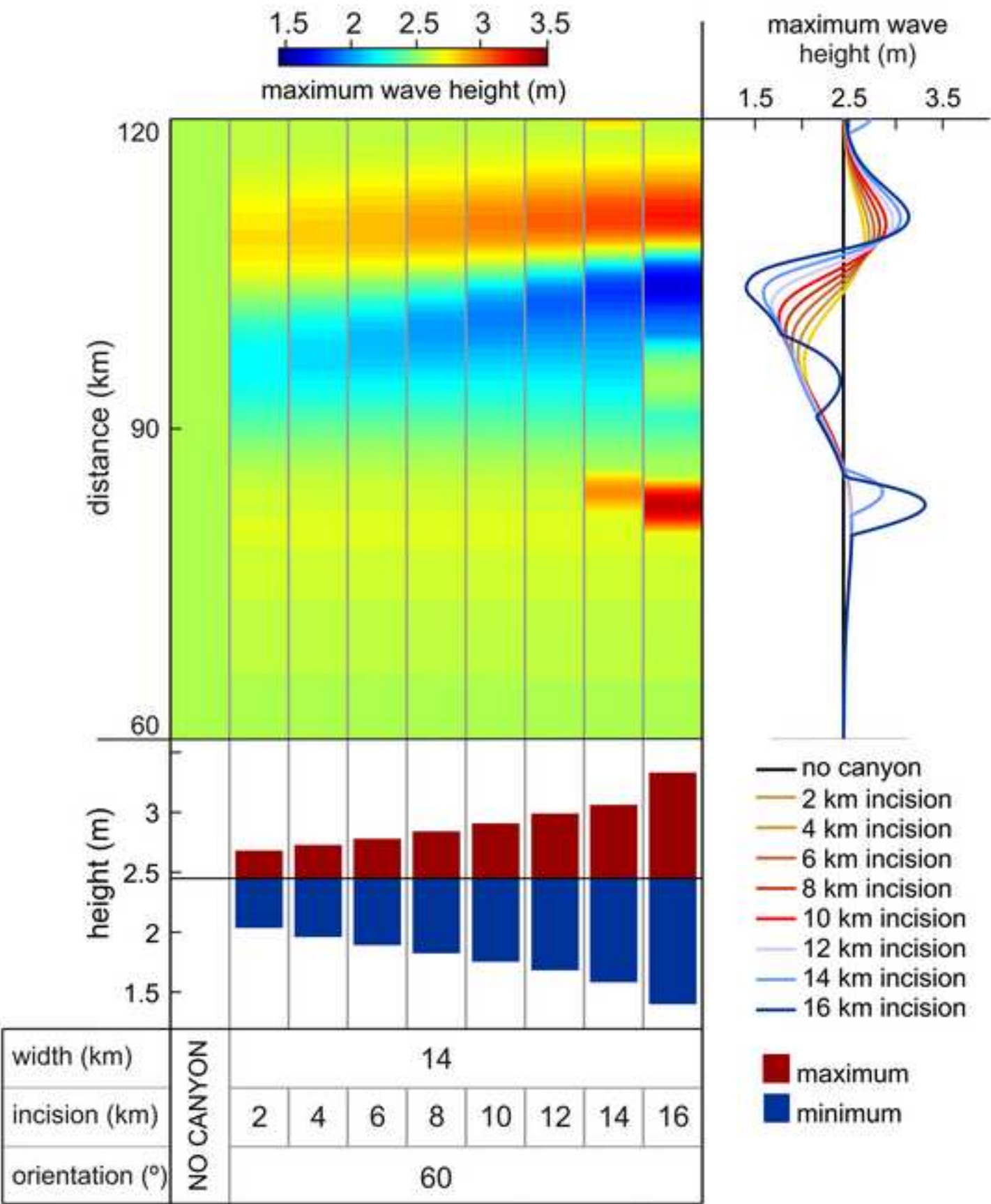


Figure14

[Click here to download high resolution image](#)

